Universität Hamburg

Fachbereich Physik

Structure and X-ray emission of the accretion shock in classical T Tauri stars

Diplomarbeit

Hans Moritz Günther

completed in Hamburg on October 31th, 2005

angefertigt unter der Betreuung von Prof. J. H. M. M. Schmitt

moritz.guenther@hs.uni-hamburg.de
Hamburger Sternwarte, Gojenbergsweg 112, 21029 Hamburg

Abstract

This work deals with young stellar objects, which are still surrounded by an accretion disk, the classical T Tauri stars (CTTS). One of the main predictions of the magnetically funnelled infall model for CTTS is the existence of a hot accretion spot. I present a computer simulation of the shock structure, which explicitly considers non-equilibrium effects. Observable quantities like the line flux are calculated for many X-ray lines. I find, that basically only two parameters of the infalling gas govern the structure of the shock, the infall velocity and the pre-shock density. Comparing to a stellar model atmosphere I estimate the depth at which the shock occurs. For shocks with velocities above 400 km/s and particle densities below 10^{11} cm^{-3} the stellar pressure causes deviations from the model used in deeper layers. Line fluxes taken from the literature for TW Hya agree with to my predictions and allow to determine the infall velocity as 525 km/s and the infall density as 10^{12} cm^{-3}. I confirm that the emitting plasma is metal depleted, but neon enhanced. The spot fills $0.1 - 0.2$ % of the stellar surface and the mass accretion rate is $1 \cdot 10^{-10} M_{\odot}$/yr. This is significantly less than results obtained previously at other wavelenghts and indicates that the shock has an inhomogeneous cross section because X-ray observation probe only the hottest part of the post-shock region whereas measurements in the UV, optical and infrared are able to detect cooler components, too. Further I calculate a lower bound on the absorbing column density $N_H = 10^{20}$ cm^{-2} from the model, which is compatible to observations. The model does not fit BP Tau well, although I tried to correct the observations for different extinction values. This is attibuted to BP Tau's known strong coronal activity. Possible values for the shock parameters are discussed, the most likely ones point to 475 km/s and 10^{12} cm^{-3}.

Zusammenfassung

Eine der wesentlichen Voraussagen der Modellvorstellung vom magnetisch kontrollierten Einfall auf klassische T Tauri Sterne (CTTS) ist eine heiße Einschlagsregion. Ich stelle hier eine Computersimulation vor, die explizit auch Nicht-Gleichgewichtsphänomene berücksichtigt. Als beobachtbare Größe wird für viele Spektrallinien im Röntgenbereich die Intensität berechnet. Es zeigt sich, dass im Wesentlichen nur zwei Parameter die Struktur des Schocks bestimmen: die Einfallgeschwindigkeit und die Dichte das einfallenden Gases vor der Schockfront. Im Vergleich mit einer Modellatmosphäre ermittle ich die Tiefe, in der sich die Schockfront bildet. Für Schocks mit Einfallgeschwindigkeiten über 400 km/s und Einfalldichten unter 10^{11} cm^{-3} bewirkt der Druck der Sternatmosphäre Abweichungen in den unteren Schichten vom hier benutzten Modell. Linienflüsse für TW Hya aus der Literatur stimmen mit meinen Vorhersagen überein und erlauben es, die Einfallgeschwindigkeit zu 525 km/s und die Dichte zu 10^{12} cm^{-3} zu bestimmen. Ich kann bestätigen, dass im beobachteten Plasma Metalle abgereichert sind, aber Neon verstärkt auftritt. Die Einschlagsregion füllt $0.1 - 0.2$ % der Sternoberfläche und der Massenfluss beträgt $1 \cdot 10^{-10} M_{\odot}$/Jahr. Diese Zahlen sind deutlich geringer als vorhergehende Resultate aus anderen Wellenlängenbereichen und deuten an, dass ein Querschnitt durch den Schock möglicherweise nicht homogen ist, weil im Röntgenbereich nur die heißesten Bereiche der Region nach dem Schock beobachtet werden, im UV, optischen oder infraroten aber auch kältere Regionen erfasst werden. Aus dem Modell berechne ich eine untere Grenze für die absorbierende Säulendichte im Schock von $N_H = 10^{20}$ cm^{-2}, dieser Wert ist mit Beobachtungen verträglich. BP Tau wird durch das Modell nicht gut beschrieben, obwohl die Beobachtungen für Absorption korrigiert wurden. Der Unterschied erklärt sich aus der schon bekannten starken koronalen Aktivität von BP Tau. Mögliche Werte für die Schock Parameter werden diskutiert, die besten sind 475 km/s und 10^{12} cm^{-3}.

Contents

Chapter 1

Introduction

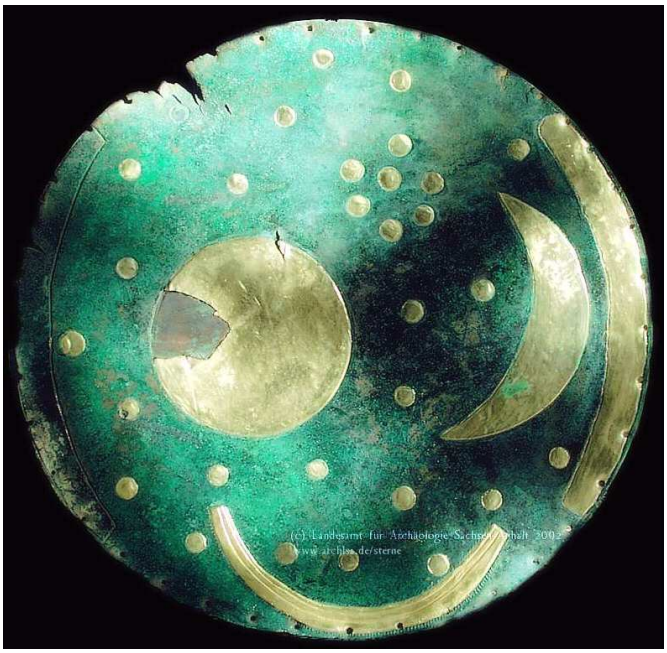

Figure 1.1: Sky disk of Nebra (Credit: Landesamt für Archäologie Sachsen-Anhalt). The group of 7 golden circles between 'sun' and 'moon' is commonly referred to as the Pleiades (Meller 2002).

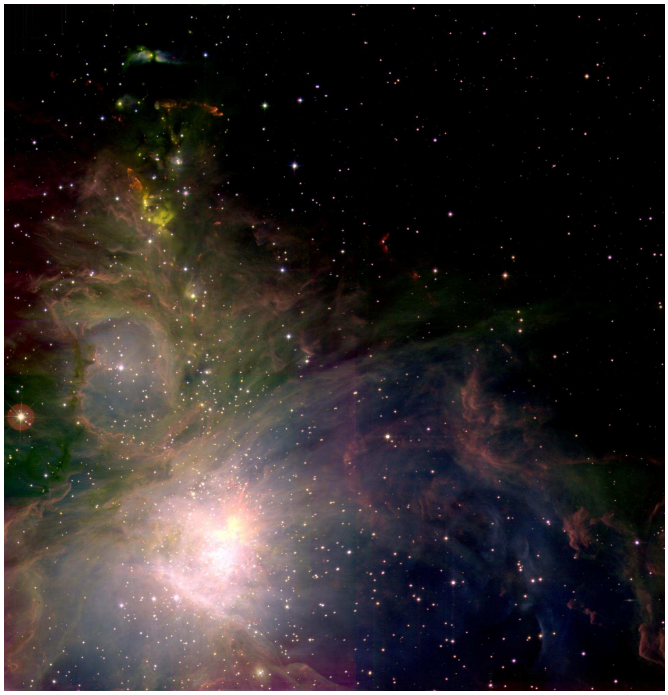

Figure 1.2: Aloha Orion, imaged in the infrared with the WFCAM of the United Kingdom Infrared Telescope (UKIRT) on Mauna Kea, is a large molecular cloud. Credit: Joint Astronomy Centre; image processing by C. Davis, W. Varricatt

1.1 Star formation

Far back in time the first humans already saw a sky very similar to our own when they looked up at night. Artifacts brought to us by archaeologists from the dawn of time like the 3600 year old sky-disk of Nebra (see figure 1.1) prove that the heavens above us were always inspected by mankind. At first the sky seems to be immovable and unchangeable, a place of gods, but using sophisticated technics we know nowadays that stars are born and die, although on eternal time scales compared to human life. They emerge from giant molecular clouds like the one in Figure 1.2. These clouds begin to collapse under their own gravitation and, because they are not homogeneous, the mass concentrates in several distinct regions, which later will become star systems, possibly binaries or even hosts for planets (a comprehensive review of the whole development can be found in Feigelson and Montmerle 1999). In this phase, which takes a few thousand years, the objects

are called 'infalling protostars'. They are still hidden in a large surrounding matter envelope, which makes it difficult to observe them, only the infrared (class 0 sources) and radio emission penetrates this barrier. Conservation of the initial angular momentum forces the structure to rotate around an axis, but nothing supports the envelope along that axis. So material falls to the plane of the evolving protostar, keeping its angular momentum, and develops a thick disk, the star becomes an 'evolved protostar'. Its age is now of the order 10^5 years, its infrarad signature class I. The material continues to contentrate in the disk plane. At the same time the star grows by mass flux from the disk. Only in the last decade evidence emerged that the disk has no direct contact to the star at a boundary layer, but an inner radius of ~ 0.5 AU (e.g. Muzerolle et al. 2003). In the 1990's theoretical considerations were published proposing a magnetically funnelled accretion stream stretching above this gap (Uchida 1983; Koenigl 1991), which is explained in more detail in section 1.2. When the envelope does not hide the system any longer, the infrared signature of the source changes to class II and it is called a classical T Tauri star (CTTS) following the prototype T Tauri (see figure 1.3) in the Taurus-Auriga star forming region. This phase lasts a few million years, until the disk is not replenished any longer from the envelope and begins to vanish. In this state the stars are weak-line T Tauri stars (WTTS). When the disk has completely dissolved either by accretion or because it was blown away by a wind (and maybe it formed even planets) the star reaches the main sequence. The energetic radiation from these stars is reflected in the remaining gas from the original cloud, giving us the opportunity to watch wonderful pictures on the night sky. An example is a young group of stars called 'Pleiades' (figure 1.4), by a strange coincidence these are also the stars depicted on the ancient sky-disk of Nebra (figure 1.1) (Meller 2002).
More massive stars go through a similar sequence as the one just described, but this work deals with relatively low mass ($M_* < 3M_\odot$) TTS. They show late-type spectra (see e.g. Muzerolle et al. 1998b, 2003). Traditionally the distinction between CTTS and WTTS is drawn by their Hα equivalent width. WTTS have weak (less than 10 Å) Hα lines, CTTS stronger ones. Nowadays more reliable tracers of accretion are known, the most prominent being the so called 'veiling'. This means that lines which are normally in absorption in comparable stars get veiled by hot continuum emission generated in the spot where the accreting matter hits the star. This has been observed in the infrared (Muzerolle et al. 2003) and in the ultraviolet (UV) band (Costa et al. 2000; Gullbring et al. 2000). According to the current model (section 1.2) the gas moves from the disk to the star at near free-fall velocity. Again this is a tracer for accretion and it has been found directly in lines as broad red wings (Edwards et al. 1994; Lamzin et al. 2004). It was explained that the gas and dust forms a disk around the star because of angular momentum conservation, now observational evidence proves that material is transferred to the star, so either the star spins up considerably or angular momentum leaves the

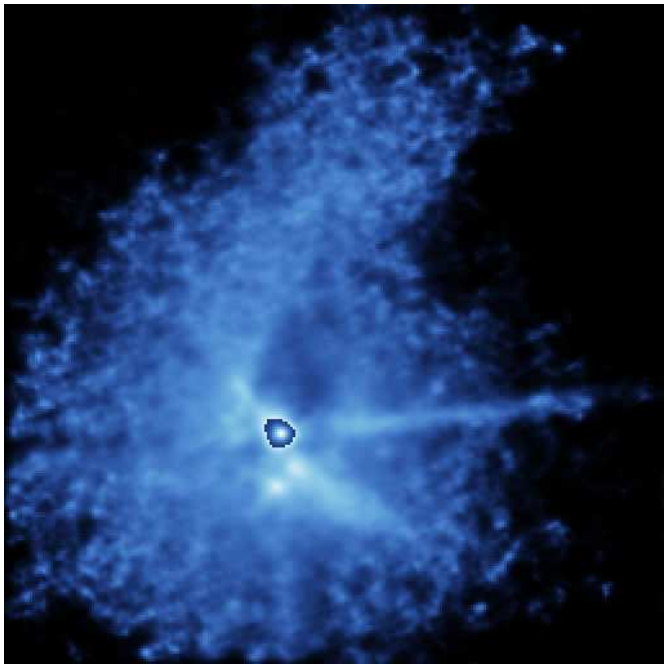

Figure 1.3: False Colour image of the collapsing gas cloud in the T Tau system. Credit: C. & F. Roddier (IfA, Hawaii), Canada-France-Hawaii Telescope.

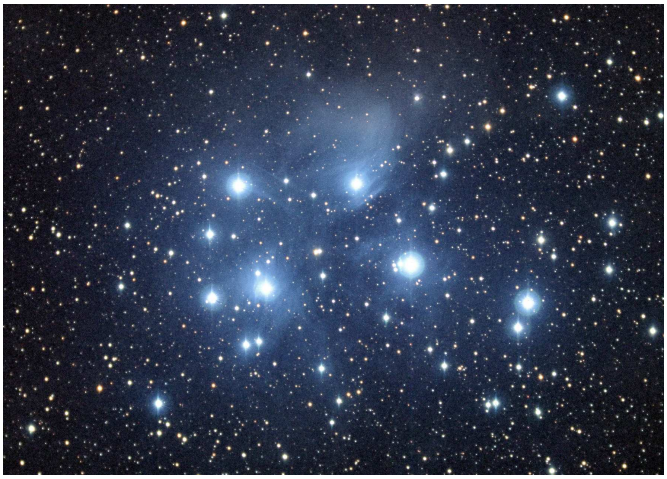

Figure 1.4: The Pleiades are young stellar objects. The blue nebula are rests of the gas cloud which reflect the star light. Credit: Aron Charad, National Optical Astronomy Observatory

system. The second possibility is realised: A wind can be detected by analysing line profiles for ions in a low ionisation state (e.g Lamzin et al. 2004; Dupree et al. 2005). All this is thought to be driven by a magnetic field, so it is plausible to check for emission at higher energies and in fact X-ray emission was detected in many CTTS using the *Einstein* (Feigelson and Decampli 1981; Feigelson and Kriss 1989) and *ROSAT* satelites (e.g. Feigelson et al. 1993; Neuhaeuser et al. 1995; Gregorio-Hetem et al. 1998). At first sight the X-ray emission seems to originate from coronal activity in a scaled-up version of our own Sun, but observations with the new generation of satelites, which provide a much better spectral resolution point to the existence of a dense plasma most likely in the accretion spot. Only two CTTS have been studied in detail so far using *Chandra* (Kastner et al. 2002) and *XMM-Newton* (Stelzer and Schmitt 2004; Schmitt et al. 2005).

1.2 The accretion model

Observations indicate, that the circumstellar disk around CTTS has an inner radius of several stellar radii (Muzerolle et al. 1998a, 2003). The current model states, that here, where the Keplerian rotation rate of the disk equals the stellar rotation period, magnetic field lines from a stellar dipole filed can penetrate the disk. The geometry is shown in figure 1.5. At the inner rim of the disk gas is ionised by radiation from the star (Glassgold et al. 2000), so it starts to interact with the magnetic field. The gravitation drags all material towards the star, but the ions are forced to follow the magnetic field lines and rise above the disk plane in an 'magnetically funnelled' accretion flow. Along the magnetic field they are accelerated gravitationally until the impact on the star with nearly free-fall velocity. Extensive theoretical models have been calculated and show that this mechanism can transport angular momentum from the star to the disk, so the star is not accelerated to unusual fast rotation (Shu et al. 1994). Furthermore, this magnetic field configuration drives simultaneously a wind from the disk (Shu et al. 2000; Konigl and Pudritz 2000).

The accretion spot is presumably located at high latitudes, but the exact position and the form of the regions is still a matter of debate. It could be a ring at constant latitude or several distinct spots. Romanova et al. (2004) have done a fully 3 dimensional magneto-hydrodynamic (MHD) simulation of the funnel flow and find two or more essentially banana shaped spots near the pole depending on the inclination of magnetic and rotational axis of the star. An example from their simulation is shown in figure 1.6. Two accretion funnels form (left panel) and the position of the spots for an misalignment between rotational and magnetical axis $\Theta = 15^\circ$ settells close the magnetic poles. The spot is inhomogeneous, density (right panel) and velocity increase towards the centre.

This general accretion model describes which density and infall velocities are to be expected in an accretion spot. The inflowing gas penetrates the stellar atmosphere until a shock front develops which heats up the gas. It emits the line and continuum radiation, that we observe as veiling. It cools down and mixes with the surrounding stellar atmosphere in the end. Only

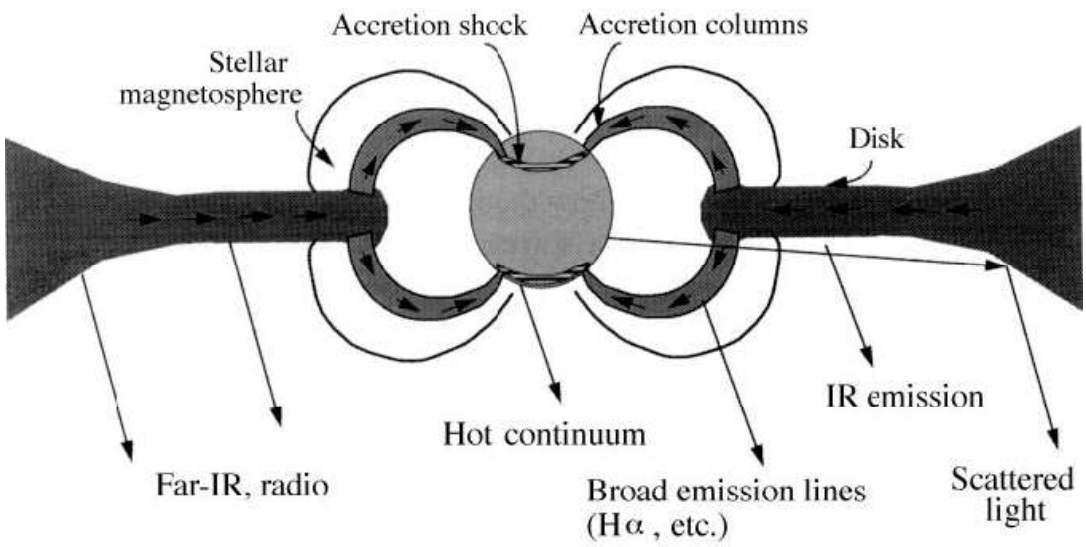

Figure 1.5: Model of disk accretion, from Hartmann (1998)

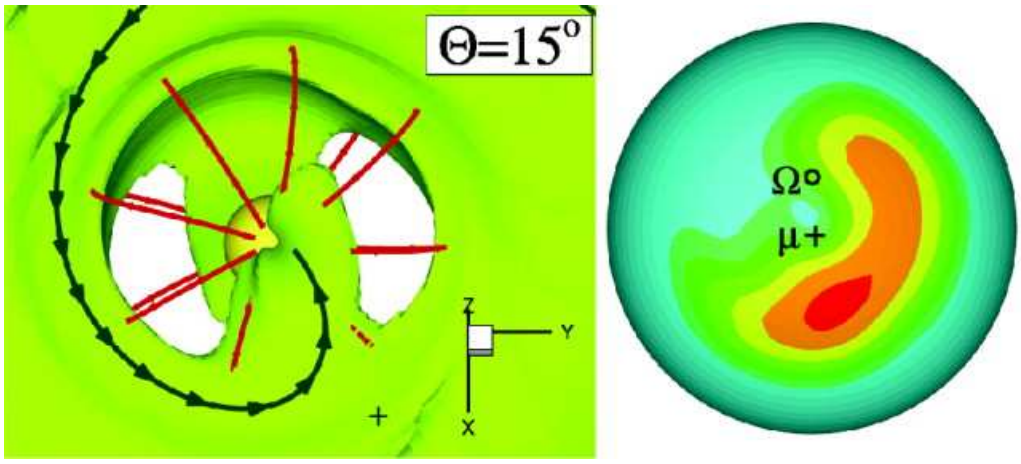

Figure 1.6: Left: Accretion funnel streams: Red marks sample magnetic field lines. The arrow follows a particle stream. Right: The shape of the accretion spot resembles a banana. μ marks the axis of the magnetic moment of the star, Ω its rotation axis and Θ the angle between them. The density of the accretion stream is colour coded from blue (low) to red (high). from: Romanova et al. (2004)

a detailed modelling of shock front and radiating region can explain the observed features. Concentrating on the optical and infrared emission Calvet and Gullbring (1998) published a successful model and similar work was done for X-ray by Lamzin (1998). Since that time the available atomic data has improved and computational contrains are lifted due to much faster hardware. In this thesis I present a new simulation of the accretion shock and the following region, which considers non-equilibrium effects, uses up-to-date databases and resolves individual lines in the X-ray region. The results presented are applied to high-resolution X-ray spectroscopy of the CTTS TW Hya (Kastner et al. 2002; Stelzer and Schmitt 2004) and BP Tau (Schmitt et al. 2005).

1.3 Plan of report

In the following section the underlying physics for the model is summarised and extensive derivations of the implemented formulas are given. At the same time necessary assumptions and simplifications are pointed out. In section 3 the structure of the implementation and its computational parameters are explained. The results are presented in section 4, first the models are analysed in general and the condition on the emitting regions are discussed, then they are applied to data from TW Hya and BP Tau. The pre-shock conditions for these stars are identified. In section 5 my findings are compared to literature values and possible physical implications are discussed. A short summary of the main points is given in section 5.4.

Chapter 2

Basic physics

In this section I derive the physical formulas, which are implemented in the simulation. The first part, section 2.1, tells about the macroscopic physics, the hydrodynamics, the second part, section 2.2, look at the physics of the single atom or ion and describes ionisation and recombination and all processes which produce radiation. In both sections the relevant simplifications are explained and discussed.

2.1 Gas dynamics

Different physical processes are important in different zones. The gravitation of the star accelerates thin gas onto the stellar surface ('pre-shock zone'). On the surface it hits the atmosphere and a strong shock develops ('shock zone'). This is called an accretion shock. In a first layer the bulk kinetic energy is converted into undirected thermal energy ('shock front'). This process is very efficient for ions but not for electrons. Two interacting fluids develop: The ions and the electrons. Energy exchange between the species is slow and therefore they are described as two different, but interacting components. This model is commonly referred to as 'Two fluid approximation'. The temperatures of ions and electrons then converge ('post-shock zone') as the gas cools down because is it emits radiation (therefore also called 'cooling zone)'.

2.1.1 Continuum treatment

If the scale height L of all relevant physical processes is much larger than the mean free path l of a single particle a continuum treatment is possible. Otherwise the gas-dynamic equation, the Boltzmann equation, needs to be solved. Only for the first case e.g. the pressure p or the particle number density n are well defined in a small volume element V as the average of some microscopic quantity of each particle.
The mean free path can be estimated by multiplying the formula for the mean free collision time t_c for charged particles from Spitzer (1965,equation 5-26) with some average velocity v:

$$l \approx v t_c \approx v \frac{0.29}{\Lambda} \frac{m^{1/2}(kT)^{3/2}}{ne^4} \approx 1 \text{ m} \tag{2.1}$$

m is the mass (e.g. of an electron), e its charge. k is Boltzmann's constant and Λ the Coulomb logarithm which is defined later (equation 2.32). (I use the thermal electron velocity for $T = 10^6$ K and $n = 10^{14}$ cm^{-3}). At this point is only important that the numerical evaluation of this formula for typical conditions for electrons gives $l \approx 1$ m. The same is true for protons because the velocity

is proportional to the inverse square root of the mass so the mean free path is independent of it. 'Typical' condition are taken from Calvet and Gullbring (1998) and Lamzin (1995) who obtain densities in the shock region of about $n \approx 10^{-11} \frac{\mathrm{g}}{\mathrm{cm}^3}$ which translates roughly into a number density of ions $n_{ion} \approx 10^{14}\mathrm{cm}^{-3}$ in their simulation of accretion shocks with temperatures $\approx 10^6$ K.

This value is much smaller than the dimension of the radiation emitting region. The viscous shock front is only of the order of a few mean free paths, so its internal structure cannot be resolved in a continuum approximation and the resulting hydrodynamical quantities will be calculated in section 2.1.5.

2.1.2 Basic equations of hydrodynamics

If the mean free path is small, all properties of the gas are described by a few macroscopic quantities. In general they depend on position $\vec{r}$ and time t. These quantities can be scalars like temperature $T = T(\vec{r}, t)$ and mass density $\rho = \rho(\vec{r}, t)$, vectors like the bulk velocity $\vec{v} = \vec{v}(\vec{r}, t)$ or tensors like the stress tensor $P_{ik} = P_{ik}(\vec{r}, t)$. To simplify the notation the dependence on space and time coordinates is no longer explicitly written.
The mass density ρ is then directly proportional to the ion number density

$$\rho = \mu m_H n_{ion} \tag{2.2}$$

m_H is the mass of a hydrogen atom. The mean molecular weight μ is a dimensionless number calculated from

$$\mu = \sum_i \xi_i \frac{m_i}{m_H} \tag{2.3}$$

where m_i is the mass of one atom, ξ_i the relative abundance of species i and i runs over all atomic species in the gas. The stress tensor P_{ik} is given by component i of the force acting on the unit surface element normal to direction k. It can be decomposed in

$$P_{ik} = -\delta_{ik} P + \pi_{ik} \tag{2.4}$$

P is the scalar thermodynamic pressure, π_{ik} the viscous stress tensor and δ_{ik} the Kronecker-δ, which equals 1 for $i = k$ and 0 otherwise. The sign difference on the right hand side arises, because P_{ik} represents forces acting on a volume element V, but the pressure P is a force acting out of the volume on its surroundings.
The equation of state for a gas, if it is known, provides a relation between preassure and temperature. For the perfect gas it reads:

$$P = nkT \tag{2.5}$$

where k is Boltzmann's constant.
The kinetic energy of a single particle is $E_{kin} = \frac{m}{2}\vec{u}^2$ with $\vec{u}$ being its speed and m its mass. For larger ensembles it is useful to decompose the velocity in a bulk part $\vec{v}$ which represents the velocity of the centre of mass and a random part which is called thermal motion $\vec{w}$. The energy per atom/ion E consists of the kinetic part

$$E_{kin} = \frac{1}{2}\mu m_H \vec{v}^2 \tag{2.6}$$

and a thermal part

$$E_{therm} = \frac{n_f}{2} kT \tag{2.7}$$

Electrons and ions have three degrees of freedom associated with the three spatial dimensions so $n_f = 3$. Especially for processes with constant external pressure it is useful to define the enthalpy $H = E_{therm} + \frac{P}{n}$ because a gas needs to exert the force P against the external pressure to expand. For a volume V this results in the work PV. So the work per atom/ion required to expand the gas from zero to the specific volume $V = \frac{1}{n}$ is $\frac{P}{n}$. For an perfect monoatomic gas:

$$H = E_{therm} + \frac{P}{n} = \frac{3}{2}kT + kT = \frac{5}{2}kT = \frac{5P}{2n} \tag{2.8}$$

In general

$$H = \frac{\gamma}{\gamma - 1}\frac{P}{n} \tag{2.9}$$

γ is the adiabatic index, which is $\gamma = 5/3$ for monoatomic gases. Now the fluxes of conserved quantities are calculated following the derivation of Shu (1991,chapter 4). $\vec{A}$ is a surface normal of the volume V pointing outward.

mass flux There is no way to produce or destroy mass, so the change of the total mass in a volume V equals the flux through its surface A.

$$\frac{d}{dt}\int_V \rho dV = -\oint_{\partial V} \rho\vec{v}d\vec{A} = -\int_V \nabla(\rho\vec{v})dV$$

The second step is done with the help of Gauß's theorem. On the left hand side integration and differentiation are exchanged to get $\frac{\partial\rho}{\partial t} + \nabla\vec{j}_m = 0$ using the mass flux

$$\vec{j}_m = \rho\vec{v} \tag{2.10}$$

This is valid for every differential volume element so it is valid everywhere. Here no fusion or fission takes place. So the number of atoms stays constant, too and it is useful to define atom/ion flux by number:

$$\vec{j} = n\vec{v} \tag{2.11}$$

momentum flux The momentum $\vec{p} = \int_V \rho\vec{v}dV$ of a fluid changes by momentum flux or by forces acting on the fluid. The pressure acts on the surface of the volume V, the gravitation is a volumetric force ($\vec{g}$ is the gravitational acceleration and points towards the gravitating mass). For momentum component i:

$$\frac{d}{dt}\int_V \rho v_i dV = -\oint_A (\rho v_i)\vec{v}d\vec{A} + \oint_{\partial V} P_{ik}dA_k + \int_V \rho g_i dV$$

This can be transformed similarly to the mass flux to reveal the momentum flux tensor as

$$j_{p_{ik}} = (\mu m_H n v_i v_k + P_{ik}) \tag{2.12}$$

energy flux In a volume V there are nV particles. The time rate of change of the total energy (kinetic and thermal) is given by the flux of energy through the surface and by the work done on this volume. Work is done by stress and gravitation. Additionally there is a heat flux $\vec{F}_{therm}$ and a radiation flux. Energy is lost by emission (with a rate Γ_{rad}) and gained by absorption (Λ_{rad}) of radiation.

$$\frac{d}{dt}\int_V n(E_{kin} + E_{therm})dV = -\oint_A n(E_{kin} + E_{therm})\vec{v}d\vec{A} + \\ \oint_A v_i P_{ik}dA_k + \int_V \rho\vec{v}\vec{g}dV - \oint_A \vec{F}_{therm}d\vec{A} + \int_V(\Gamma_{rad} - \Lambda_{rad})dV$$

The equation for the energy flux per atom/ion

$$\vec{j}_E = (E_{kin} + E_{therm})\vec{v} - \vec{v}\frac{P_{ik}}{n} + \frac{\vec{F}_{therm}}{n} \tag{2.13}$$

now looks like

$$\frac{d}{dt}\left[n(E_{kin} + E_{therm})\right] + \frac{\partial}{\partial x_k}(nj_{E_k}) = \rho\vec{v}\vec{g} + \Gamma_{rad} - \Lambda_{rad}$$

From standard thermodynamics the adiabatic speed of sound c is known as

$$c = \sqrt{\frac{\gamma PV}{\mu m_H}} = \sqrt{\frac{\gamma kT}{\mu m_H}} \tag{2.14}$$

In media streaming with some bulk velocity v it is useful to define the Mach number M as the ratio between bulk velocity and speed of sound

$$M = \frac{v}{c} \tag{2.15}$$

because there are fundamental differences between subsonic ($M < 1$) and supersonic ($M > 1$) motions.

2.1.3 Simplifying assumptions

In order to do the simulation some approximations and assumptions are necessary. They are described here and their applicability is discussed if possible a priory.

Direction of flux and choice of coordinate system

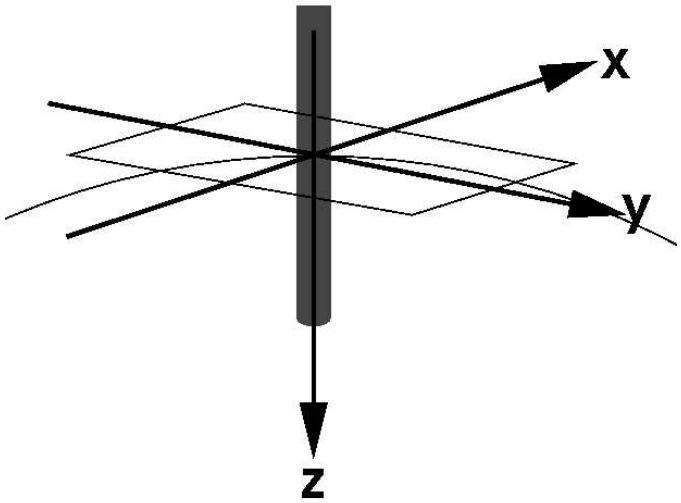

Figure 2.1: The coordinate system: The z-axis points inward and material flows along this direction.

The spatial extent of the accretion region is very small compared to the total stellar surface. This has been shown by previous simulations (Lamzin 1995; Calvet and Gullbring 1998; Romanova et al.

2004) and confirmed by observations (Calvet and Gullbring 1998; Costa et al. 2000; Muzerolle et al. 2000; Stelzer and Schmitt 2004; Schmitt et al. 2005). The surface can be taken as flat and the gas moves normal to it. The origin of the coordinate system is placed at the accretion shock front with the positive direction of the z-axis towards the centre of the star (see figure 2.1). Assuming no gradients and no flux parallel to the surface, all partial derivatives in the x- and y-direction are zero. Obviously this cannot be true everywhere because the accretion column is finite and has a surface with gradients towards the normal stellar atmosphere, but it greatly simplifies the calculations. Surface effects include thermal and radiative conduction or anisotropy pressure. If the diameter of the accretion region is large compared to its depth in z direction, then surface effects should be small. Accretion spot sizes from the references cited above and a shock depth from this simulation (setion 4.1.5) indicate that condition is easily satisfied.

Time dependence

In the model there is no explicit time dependence. Everything is in a quasi static state. This means the structure of the shock does not change with time, e.g. the energy contained in a specified depth is constant and because of that not only the energy itself is conserved, but also the energy flux. It is questionable if such a state really exists or if turbulent fluxes create an ever changing structure. On the one hand the high infall velocities contain enough energy to fuel turbulent phenomena, but on the other hand they should quickly wash out small fluctuations. Under assumption of a quasi static state there are no temporal gradients and all partial derivatives to time can be set to zero. This also simplifies total time derivatives (written in one dimension).

$$\frac{d}{dt} = \frac{\partial}{\partial t} + \frac{\partial z}{\partial t}\frac{\partial}{\partial z} = v\frac{\partial}{\partial z} \tag{2.16}$$

Magnetic fields and heat conduction

As described in section 1.2 the current model states that the infalling material is channelled by magnetic field lines and moves along them, so the direction of the magnetic flux is parallel to the bulk motion and there is no magnetic force. So it is sufficient to use normal hydrodynamics and not magneto-hydrodynamics. Nevertheless, there will be a small scale chaotic magnetic field. This suppresses free electron movement and consequently there is no or only little heat conduction, since in a plasma the electrons transport most of the heat due to their longer mean free path (Zel'Dovich and Raizer 1967). I use $F_{therm} = 0$ in the simulation. Lamzin (1998) includes a small magnetic field in his energy and momentum equations and finds its strength is not coupled to macroscopic shock parameters. In section 4.3 I will discuss the importance of heat conduction if it is not suppressed.

Gravitation

Gravitational forces are negligible. The difference of the potential energies for an ion between the stellar surface and the bottom of the accretion region in a few hundred kilometers depth is only 0.2 eV, which is very small compared to the thermal energy of a few eV and the kinetic energy of hundreds of eV. The electron mass is much smaller and so the potential and kinetic energy are three orders of magnitude smaller, hence gravitational energy is very small compared to thermal and kinetic, too.

Viscous forces

Internal stress is small in thin gases and is neglected. On the right hand side of equation (2.4) I keep only the scalar component.

2.1.4 Simplified fluxes

These approximations simplify the equations of the fluxes. Scalar expressions representing the z-component of a quantity are used instead of vector expressions, because there is no flux and no gradient in x and y direction:

$$\vec{j}_m = \begin{pmatrix} 0 \\ 0 \\ j_m \end{pmatrix}$$

So equation (2.10) reads now

$$j_m = \rho v \tag{2.17}$$

or the particle flux density

$$j = nv \tag{2.18}$$

The momentum flux (2.12) simplifies to

$$j_p = \mu m_H n v^2 + P = \mu m_H n v^2 + nkT \tag{2.19}$$

In the two fluid approximation the total momentum flux is the sum of the ion and the electron component. The term $m_{electron}v^2$ can be neglected because $m_{elec} \ll m_{ion}$.

$$j_p = \mu m_H n v^2 + nkT_{ion} + n_{elec}kT_{elec} \tag{2.20}$$

The energy flux per atom/ion (2.13) gives

$$j_E = (E_{kin} + E_{therm})v + \frac{vP}{n} = v(E_{kin} + H) \tag{2.21}$$

2.1.5 The shock front

The shock front is very thin. It takes only a few mean free paths for the ions to decelerate and transfer their kinetic energy to thermal motion. Other degrees of freedom than thermal ones are not excited so fast, so the ionisation state does not change. Zel'Dovich and Raizer (1967) define the thickness δ of the shock front as

$$\delta = \frac{v_0 - v_1}{(\partial v/\partial x)_{max}}$$

Here v_0 is the bulk velocity before the gas reaches the shock front and v_1 after passing through the front. They also show that the order of magnitude for the front can be approximated in terms of the Mach number M (equation 2.15) and the mean free path l (chapter 7 Zel'Dovich and Raizer 1967):

$$\delta \approx l\frac{M}{M^2 - 1}$$

For strong shocks the thickness seems to vanish, but of course there is a lower bound. The thickness cannot be shorter than a few mean free paths because there obviously need to be interactions between the particles to decelerate them. Therfore, the volume of the viscous shock front is small

and the internal structure unimportant, which allows a treatment as mathematical discontinuity. The fluxes of the conserved quantities mass (2.17), momentum (2.20) and energy (2.21) are sufficient to calculate the state behind the shock front. This derivation follows the book of Zel'Dovich and Raizer (1967) (chapter 7)

$$\rho_0 v_0 = \rho_1 v_1 \tag{2.22}$$
$$P_0 + \rho_0 v_0^2 = P_1 + \rho_1 v_1^2 \tag{2.23}$$
$$h_0 + \mu m_H v_0^2 = h_1 + \mu m_H v_1^2 \tag{2.24}$$

The state before the shock is marked by index 0, behind the shock front by index 1. Equation (2.24) is rewritten in terms of ρ, v and P with (2.8).

$$\frac{5P_0}{2\rho_0} + \frac{v_0^2}{2} = \frac{5P_1}{2\rho_1} + \frac{v_1^2}{2} \tag{2.25}$$

In equation (2.22) ρ_1 can be eliminated and the resulting equations are written in terms of dimensionless variables:

$$\bar{v} = \frac{v_1}{v_0} \quad \bar{P} = \frac{P_1}{P_0} \quad x = \frac{P_0}{\rho_0 v_0^2}$$

x contains only the variables before the shock and is known. Now (2.23) is

$$x + 1 = \bar{P}x + \bar{v}$$

Substituting this in (2.25) leads to

$$5x + 1 = 5\bar{v}(x + 1) - 4\bar{v}^2$$

and

$$0 = 4\bar{v}^2 - 5 \cdot (x + 1)\bar{v} + (5x + 1)$$

with two solutions

$$\bar{v} = \frac{5x + 1}{4} \text{ and } \bar{v} = 1$$

The second solution describes a situation with steady flow and without shock, the first one yields the desired result. All parameters behind the shock can now be calculated:

$$P_1 = \frac{3\rho_0 v_0^2 - P_0}{4} \tag{2.26}$$
$$v_1 = \frac{P_0 - P_1}{\rho_0 v_0} + v_0 \tag{2.27}$$
$$\rho_1 = \frac{\rho_0 v_0}{v_1} \tag{2.28}$$

These equations are called 'Rankine-Hugoniot-jump conditions'.
There are much less viscous forces between electrons. Therefore the electronic component is not processed via the Rankine-Hugoniot conditions, but to first approximation just gets compressed adiabatically. This means the temperature raises according to

$$T_{e_1} = T_{e_0}(\frac{\rho_1}{\rho_0})^{(\gamma-1)} \tag{2.29}$$

with γ being the adiabatic index like in equation (2.9). Evaluation these equations shows that the temperature of the electrons is orders of magnitude lower then the ion temperature after the accretion shock front.

2.1.6 Post-shock region

While passing the shock front the gas decelerates to subsonic velocities and the ions are much hotter then the electrons. Therefore, heat is transfered from the ionic to the electronic component in the post-shock zone. Simultaneously the gas radiates and cools down, so the energy of the gas is no longer conserved and equation (2.21) is not valid anymore as it does not include the radiative energy flux. Instead the energy per particle must be described by an ordinary differential equation (ODE) for the ions and another for the electrons.
Starting from the thermodynamic relation

$$Td\Sigma - PdV = dU \tag{2.30}$$

where Σ denotes the entropy and U the internal energy I will derive the ODE for the ionic component. For simplification everything will be expressed per heavy particle (atom or ion).
$Td\Sigma = dQ$ is the flux of heat through the boundaries of the system. The system "ions" looses heat by collisions with the colder electrons. Microscopically heat is just the energy of unordered motion. The fraction of the kinetic energy of a single particle transferred per collision cannot exceed the mass ratio $\frac{m_{elec}}{m_{ion}}$. It is most efficient for the light ions. Hydrogen is by far the most abundant element and its atomic mass number is one. The hydrogen ions have a much larger cross sections than the atoms and hydrogen is nearly completely ionised in the whole shock region anyway, so contributions of heavier elements are neglected. Zel'Dovich and Raizer (1967,Chapter VII, §10) give the heat outflow ω_{ei} per unit volume per unit time as (in cgs-units)

$$\omega_{ei} = \frac{3}{2}kn\frac{T_{ion} - T_{elec}}{T_{elec}^{3/2}}\frac{\Lambda}{252}$$

The number density of hydrogen ions is the number density of all heavy particles n multiplied with the abundance ξ_H of hydrogen and the ionisation fraction x_H^1 (these quantities are defined in section (2.2) more strictly), so

$$\omega_{ei} = \frac{3}{2}k\xi_H x_H^1\frac{T_{ion} - T_{elec}}{T_{elec}^{3/2}}\frac{\Lambda}{252} \tag{2.31}$$

Λ is the Coulomb-logarithm

$$\Lambda \approx 9.4 + 1.5\ln T_{elec} - 0.5\ln n_{elec} \tag{2.32}$$

In the last two equations temperatures are meant to be in Kelvin. Substituting (2.31) in (2.30) written per heavy particle and taking the time derivative results in

$$\frac{dU}{dt} + P\frac{dV}{dt} = T\frac{d\Sigma}{dt} = \frac{dQ}{dt} = \frac{1}{n}\omega_{ei}$$

Using the stationary condition (2.16) transforms this in an ordinary differential equation only dependent on x. Differentiation with respect to x will be indicated by $'$.

$$vU' + PvV' = \frac{1}{n}\omega_{ei}$$

The internal energy U is in this case the thermal energy from equation (2.7), the pressure P can be rewritten with (2.5). The specific volume V is the inverse of the number density $V = \frac{1}{n}$.

$$v\left(\frac{3}{2}kT_{ion}\right)' + vnkT_{ion}\left(\frac{1}{n}\right)' = -\omega_{ei}x_e n \tag{2.33}$$

It is convenient to write the electron number density as $n_{elec} = x_e n$. x_e is the number of electrons per heavy particle.
The derivation for the electron component is similar. As the heat loss of the ion gas is a gain for the electrons this term enters with opposite sign and an additional loss term Q_{col} due to radiation appears.

$$v\left(\frac{3}{2}x_e k T_{elec}\right)' + v x_e n k T_{elec}\left(\frac{1}{n}\right)' = (\omega_{ei} - Q_{col}) x_e n \tag{2.34}$$

In principle Q_{col} depends on the local temperature, density and ionisation state of the gas. These effects are small and they are neglected in solving the ODEs for small time steps. There are four independent variables left (n,v,T_{ion} and T_{elec}). n can be eliminated easily because of particle number conservation (equation 2.18). The momentum flux conservation (2.20) is a second algebraic equation and can be solved for v. Unfortunately it is quadratic in v with two solutions. I will use the following abbreviations

$$\begin{aligned} M &= \mu m_H \\ \tau_i &= k T_{ion} \\ \tau_e &= x_e k T_{elec} \\ \tau &= \tau_i + \tau_e \end{aligned} \tag{2.35}$$

These solutions are

$$v_\pm = \frac{j_p \pm \sqrt{j_p^2 - 4Mj^2\tau}}{2Mj} \tag{2.36}$$

v_+ and v_- are equal for $v_0 = \sqrt{\frac{\tau}{M}}$ which is the isothermal speed of sound. It is lower than the adiabatic one in (2.14). For subsonic velocities v_- is the physical decelerating solution. v_+ is the accelerating branch. I will need the derivative of v with respect to x.

$$\frac{dv}{dx} = \frac{j\tau'}{\sqrt{j_p^2 - 4M\tau j^2}} = \frac{j\left(\tau_i'\tau_e'\right)}{\sqrt{j_p^2 - 4M\tau j^2}} \tag{2.37}$$

Now (2.33) and (2.34) can be rewritten:

$$\frac{3}{2}\frac{\tau_i'}{\tau_i} + \frac{v'}{v} = -\frac{\omega_{ei} x_e j}{\tau_i v^2} \tag{2.38}$$

$$\frac{3}{2}\frac{\tau_e'}{\tau_e} + \frac{v'}{v} = -\frac{x_e j}{\tau_e v^2}(\omega_{ei} - Q_{col}) \tag{2.39}$$

$$\tag{2.40}$$

Solving for τ_i' and τ_e' leaves a set of two coupled ODEs which needs to be solved numerically.

$$\tau_i' = \frac{\frac{x_e j}{v^2}\left[-\frac{\omega_{ei}}{\tau_i} - \frac{2j}{3v\sqrt{j_p^2 - 4M\tau j^2}}\left(\omega_{ei}\left(1 + \frac{\tau_e}{\tau_i}\right) - Q_{col}\right)\right]}{\frac{3}{2\tau_i} + \frac{j}{v\sqrt{j_p^2 - 4M\tau j^2}}\left(1 + \frac{\tau_e}{\tau_i}\right)} \tag{2.41}$$

I state τ_e' here without backsubstituting τ_i since the formula is complex.

$$\tau_e' = \tau_i'\frac{\tau_e}{\tau_i} + \frac{2x_e j}{3v^2}\left[\omega_{ei}\left(1 + \frac{\tau_e}{\tau_i}\right) - q_{col}\right] \tag{2.42}$$

To extract the physical parameter T_{elec} x'_e must be known from the ionisation and recombination processes (given in section 2.2).

$$T'_e = \frac{\tau'_e}{x_e k} - T_{elec}\frac{x'_e}{x_e}$$

2.2 Microscopic physics

Observations in astrophysics measure radiation, which is emitted by several different processes. They can be separated into free-free, free-bound and bound-bound processes. They all depend on the ionisation and excitation state of the atom or ion in question and possibly on some macroscopic parameters namely the electron density.
The abundance ξ of all elements stays constant, because in the accretion shock no fission or fusion takes place. The abundance of element A is defined as

$$\xi^A = \frac{n^A}{n} \tag{2.43}$$

where n is the number density of all heavy particles and n^A the number density of atoms and ions with atomic number A.
An atom with element number A can be in $A+1$ different ionisation states. By convention the neutral state is labeled as 'I', e.g. 'C I'. The fraction of all atoms of element A with ion charge Z is written x_Z^A. All ions are in exactly one state at any time so

$$\sum_{Z=0}^{A} x_Z^A = 1 \tag{2.44}$$

for all A. Using equation (2.43) the number density n_Z^A of ions with charge Z and element number A can be calculated as

$$n_Z^A = n\xi^A x_Z^A \tag{2.45}$$

It changes when ionisation or recombination processes occur.
This section lists the simplifications in the treatment of the microscopic physics and explains the different processes which are considered in the simulation.

2.2.1 Simplifications

Many different processes take place in a plasma. To model the overall behaviour the physically most important ones need to be selected. In this simulation the plasma is treated as purely collision-dominated. The collision rate is small enough so that excitation and deexcitation processes are much faster than ionisation and recombination, therefore they can be treated separately. At each time the excitation is taken to be in its equilibrium state.

Velocity distribution

According to Spitzer (1965,chapter 5.3) particle velocities are Maxwellian distributed after a few mean free path lengths. His formula for the collision time scale t_c of charged particles like electrons or protons with themselves is

$$t_c = \frac{0.290}{\Lambda}\frac{m^{1/2}(kT)^{3/2}}{ne^4} \text{ (in cgs-units)} \tag{2.46}$$

Here e is the elementary charge and all other symbols have their usual meaning. For hydrogen ions the time scale is (neglecting the dependence of Λ on T and n, see equation (2.32)):

$$t_c(\text{hydrogen ions}) \sim 8 \cdot 10^{-6} \left(\frac{T}{10^6\ K}\right)^{3/2} \left(\frac{10^{14}/\text{cm}^3}{n}\right)\ [\text{in s}] \tag{2.47}$$

Right behind the shock front the temperature may be higher and the density two orders of magnitude lower, but even in this case the ions will be Maxwell distributed after a few hundred meters, electrons arrive at a Maxwellian distribution about 50 times faster than ions, because their mass is much lower. In the shock front itself they stay cool and keep their old Maxwell distribution.
A Maxwellian velocity distribution $\Phi(v)$ is characterised by its temperature T:

$$\Phi(v)dv = \frac{4}{\sqrt{\pi}} \left(\frac{m}{2kT}\right)^{\frac{3}{2}} v^2 \exp\left(\frac{v^2 m}{2kT}\right) dv \tag{2.48}$$

where k is the Boltzmann constanta and m the mass of the particle. The most probable velocity is $v_{prob} = \sqrt{\frac{2kT}{m}}$. Hydrogen, the lightest atom, is already ~ 1800 times more massive than an electron, therefore its velocity can be neglected if the temperatures of electrons and ions are similar. In this approximation the relative velocity $\vec{v}_{rel}^2$ between electron and proton is just the electron velocity. In (2.48) the velocity contributes only quadratically and the Maxwellian averaged of a quantity a is written $< a >$. The averaged quadratic relative velocity is

$$\begin{aligned} \vec{v}_{rel}^2 &= < (\vec{v}_{ion} - \vec{v}_{elec})^2 > \\ &= < v_{ion}^2 + v_{elec}^2 - 2\vec{v}_{ion}\vec{v}_{elec} > \\ &= < v_{ion}^2 > + < v_{elec}^2 > -2 < \vec{v}_{ion}\vec{v}_{elec} > \end{aligned} \tag{2.49}$$

$< \vec{v}_{ion}\vec{v}_{elec} >$ equals 0 for uncorrelated velocities. This can be used to fold the two Maxwell distributions for electrons and ions. The result is again a Maxwell distribution and can be treated as if only the electrons move with the temperature $T_{e_{eff}} = T_{elec} + T_{ion}\frac{m_{elec}}{m_{ion}}$.

Electromagnetic fields

Electric and magnetic fields are neglected. This is possible because the electrons have a high mobility and any effective charge density is balanced quickly by in- or outflow of electrons. Zel'Dovich and Raizer (1967,in chapter VII,§13) argue that there is actually a small charge separation in the shock wave only on length scales of the Debye-radius which is smaller than $\approx 10^{-2}$ cm for typical conditions in the accretion plasma. It was already mentioned that magnetic fields are interesting globally, because they channel the material onto the accretion spot, but the field strength is too small to produce effects, which are directly observable in X-rays. In this model electrons and ions move with identical bulk velocity so there is no current which could produce a strong local magnetic field.

Optical depth

Photons emitted in an optically thick plasma are scattered after emission or absorbed and later reemitted. This can change the spectral distribution and is an energy source in the absorbing regions. Much simpler are optically thin plasmas and in this model the assumption is made that

every photon escapes from the plasma. Hot plasma usually has a very small continuum opacity and the X-ray emitting region is not very large. However, radiation may be reprocessed in the accretion column and high energy photons will be absorbed and create a region of ionised plasma in front of the shock (Lamzin 1995; Calvet and Gullbring 1998).

2.2.2 Ionisation state

Ions are ionised by electron collisions (bound-free) and recombine by electron capture (free-bound). So the number density of ionisations $n_{i\to i+1}$ per unit time from state i to $i+1$ is proportional to the number density of ions n_i in ionisation state i and the number density of electrons n_e. For convenience I do not write a superscript identifying the element in question.

$$n_{i\to i+1} = R_{i\to i+1} n_e n_i \tag{2.50}$$

Recombination is the reverse process

$$n_{i\to i-1} = R_{i\to i-1} n_e n_i \tag{2.51}$$

$R_{i\to j}$ is called a rate coefficient. It describes ionisation for $j = i+1$ and recombination for $j = i-1$. For element z $R_{1\to 0} = R_{z+1\to z+2} = 0$ because 1 represents the neutral atom which cannot recombine any further and $z+1$ the completely stripped ion which cannot lose more electrons. The cross section σ for each process depends not only on the ion, but also on the relative velocity of ion and electron as well. The rate coefficient is proportional to the Maxwellian averaged cross section:

$$R \sim < \sigma(v) > \tag{2.52}$$

On the one hand the number of ions in state i decreases by ionisation to $i+1$ or recombination to $i-1$, on the other hand it increases by ionisations from $i-1$ to i and by recombination from $i+1$. So for each element z there is a set of equations

$$\frac{dn_i}{dt} = n_e(R_{i-1\to i}\, n_{i-1} - (R_{i\to i+1} + R_{i\to i-1})\, n_i + R_{i+1\to i}\, n_{i+1}) \tag{2.53}$$

Through the factor n_e the equations for all elements are coupled and together with the condition of number conservation they provide a complete system of coupled differential equations. This can be simplified considerably with the assumption that n_e is constant (which is always true if hydrogen is completly ionised) for small time intervals Δt because this results in one independent set of equations per element. Dividing by the number density of the element in question and using 2.45 leads to

$$\frac{dx_i}{dt} = n_e(R_{i-1\to i}\, x_{i-1} - (R_{i\to i+1} + R_{i\to i-1})\, x_i + R_{i+1\to i}\, x_{i+1}) \tag{2.54}$$

This approximation is good if most hydrogen is ionised because its abundance ξ^H is much larger than for any other element. This is the case in the post-shock zone and I assume that this is true already in front of the shock (as shown in Lamzin 1995; Calvet and Gullbring 1998).
In a quasi static state all time derivatives vanish. The $z+1$ equations for element z can be written in matrix form. Only z of them are linearly independent, so the first row can be replaced with a the normalisation condition (2.44). Here the arrows are left out for short notation, R_{12} should be

read as $R_{1\to 2}$.

$$\begin{pmatrix} 1 \\ 0 \\ 0 \\ \vdots \end{pmatrix} = \begin{pmatrix} 1 & 1 & 1 & 1 & \cdots \\ n_e R_{12} & -n_e(R_{21}+R_{23}) & n_e R_{32} & 0 & \cdots \\ 0 & n_e R_{23} & -n_e(R_{32}+R_{34}) & n_e R_{43} & \cdots \\ \vdots & \ddots & \ddots & \ddots & \ddots \end{pmatrix} \begin{pmatrix} x_1 \\ x_2 \\ x_3 \\ \vdots \end{pmatrix} \tag{2.55}$$

There are two important ways to ionise an atom or ion (Raymond 1988). On the collision the electron can directly ionise (direct ionisation) or excite the target above the ionisation threshold and instead of falling back to its groundlevel the excited electron can then autoionise (excitation - autoionisation). Mazzotta et al. (1998) use a single fitting formula from Arnaud and Rothenflug (1985) and Arnaud and Raymond (1992) to calculate the rate coefficients. Recombination is possible in three ways (Raymond 1988): Direct recombination means that the electron is captured to a low state. Its energy is emitted by a photon. Instead it could loose at least some energy by exciting an electron of the target. If that electron is emitted again the net result is just elastic scattering, but if it is still bound there are now two excited electrons which will emit photons. This is called a dielectronic recombination. The third possibility is a charge transfer reaction, where one electron passes from one atom, usually hydrogen or helium, to a higher ionised ion. This effectively raises the ionisation of the first and lowers it for the second. Raymond (1988) states that this may be an important channel in many astrophysical applications, but Arnaud and Rothenflug (1985) argue that in hot plasmas there are not enough neutral atoms. All these are free-bound processes.

2.2.3 Excitation state

Spectral lines are excited mostly by electron collisions. They decay in one or more steps to the ground state and emit photons in spectral lines. The line strength of several lines depends on collision strength and the statistical weight of ground state (Raymond 1988). The energy of the transition determines the wavelength of the line. These constants can be calculated from theoretical considerations and from measurements. They are compiled in a number of databases like CHIANTI (Dere et al. 1998; Young et al. 2003) or APED (Smith et al. 2001). Brickhouse (1999) and Raymond (1988) point out how important the accuracy of theses rates is to obtain reliable simulations and strongly advice to use up to date databases.
Not all deexcitations produce lines. Some emit two photons and the energy per photon can vary. This is the so called 'Two photon continuum'.
These processes are summarised as bound-bound reactions.

2.2.4 Free-Free-Reactions

In a plasma electrons that pass ions are accelerated in their electric field. Maxwell's equations show that this causes the emission of Bremsstrahlung. It is possible to calculate classical and semi-classical approximations. The loss is proportional to the square of the ion charge, but for ions that are not completely stripped, electrons with higher energy may impact more closely to the nucleus and feel a less screened field. I use the implementation of CHIANTI (Young et al. 1998). For very hot plasmas (temperatures above 10^7 K) this is the dominant source of emission (Raymond 1988).

Chapter 3

Program design and verification

This section covers the design of the program, its internal structure and the data sources for physical constants in section 3.1. It then describes the tests which check the correctness of the implementation in 3.2 and finishes with a discussion about the influence of some programme parameters on the execution time an the accuracy of the simulated results (section 3.3).

3.1 Program design

3.1.1 Design concept and programming language

The task set for this thesis consists of two parts. Firstly I needed to write the simulation program and secondly there is the analysis of the results. The simulation part requires a language with full programming capability in a stable and fast environment. The existence of many canned solvers for differential equations and efficient matrix handling is an advantage. There is a software package which does the full excitation/deexcitation calculations and delivers the line intensities: CHIANTI (Young et al. 2003; Dere et al. 1997). This is published in IDL (Interactive data language). It would have been time consuming and error prone to redo this in a different language and it is always difficult to construct complex interacting programs from different underlying systems. Additionally IDL is well suited to do data analysis and plotting. Therefore, I decided to implement as much as possible in IDL. For the progam design this means that no change of any data format is necessary between simulation and analysis. Data can be saved in ASCII or native IDL format and some information can be kept in variables over the whole time. A huge library of mathematical routines for equation solving is supplied and arrays are a native data format which can be handled fast and conveniently. On the other hand, modern object oriented design technics are only partially supported. IDL supplies basic objects in the version 6.1, but some methods do not work in an object oriented environment. Instead data is passed via common blocks without explicit control over their lifetime. I could implement only one building block as an actual object: The output. All data to be kept is passed into this object which organises the structure and the sorting in different files. There are some arguments to use dimensionless parameters of order unity, but this approach conflicts with CHIANTI which requires density and temperature input in physical units. For consistency I chose to use cgs-units throughout the program.

The implementation is simplified by the fact that the physics falls conveniently into two parts. I described the physical basis of the hydrodynamic part in 2.1 and the microscopic part in 2.2. In principal both systems of equations are coupled via the electron density, but in equation 2.54 the advantage of keeping it constant for small time steps is obvious. If this approach is taken already for the microscopic physics alone there is no reason to keep the coupling to the hydrodynamics. In this way, the largest system of coupled ODEs, which needs to be solved, is the rate equation for the heaviest element consisting of ~ 30 equations, which is easily managable by typical canned ODE solvers.

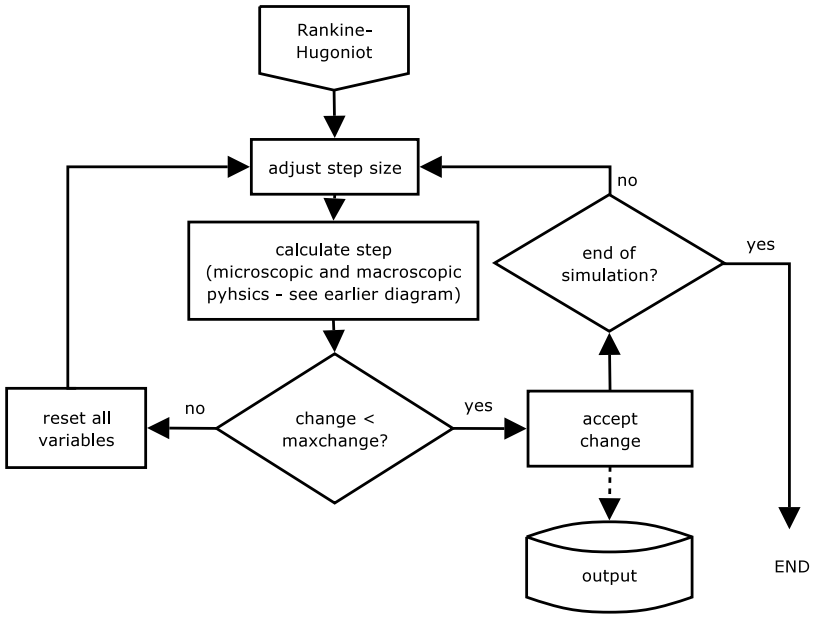

Figure 3.1: Diagram of programme control, data flow (arrows) and output data (dashed arrows). See text for details

3.1.2 Numerical simulation

The simulation needs physical parameters of the inflowing gas as input (gas density and speed, temperatures of ion and electron component, abundances and ionisation states). In the shock front it is compressed according to the analytical Rankine-Hugoniot jump conditions. After passing through this phase the numerical simulation starts. At the beginning of every time step the ionisation state changes via ionisation and recombination. According to this the CHIANTI code calculates the radiative losses. This in turn is an input to the procedure 'hydrodynamics', which solves the gas dynamic equations. In this manner the program calculates the shock structure from the surface deeper into the stellar atmosphere and after every step the data is sent to the output object. The simulation stops when the gas cools down to 12000 K (This is called the 'maximum depth' of the shock.) In section 4.1.5 it will be shown that the gas cools very fast in the end and because of that the temperature which stops the simulation is unimportant. The results are written to disk and program control returns to the calling level. In the flow chart 3.1 the program and data flow is shown.

In decoupling the hydrodynamic and the ionisation equations an inaccuracy is introduced. This is smaller for smaller step sizes, because then the results of the hydrodynamics calculation affect the microscopic part earlier and the other way round. On the other hand, smaller steps are computationally more time-consuming. An adaptive step size control adjusts the spatial size of steps in such a way that the maximum change of all hydrodynamic variables or ionisation states per step is smaller than a given maximum value. Figure 3.2 illustrates how it is implemented. The basic concept from 3.1 is extended. After processing the Rankine-Hugoniot conditions the initial step size is set. Then the program simulates a complete step (microscopic and macroscopic physics). If any variable changes by more than the specified maximum (a program parameter) this step is discarded, the step size reduced and the step recalculated. Otherwise it is accepted and the data given to the output object. Now there is a check if one of the aborting conditions is matched. The normal stop occurs if the temperature drops below 12000 K. In this region certainly no X-ray emission is formed any longer and the structure is dominated by photo-

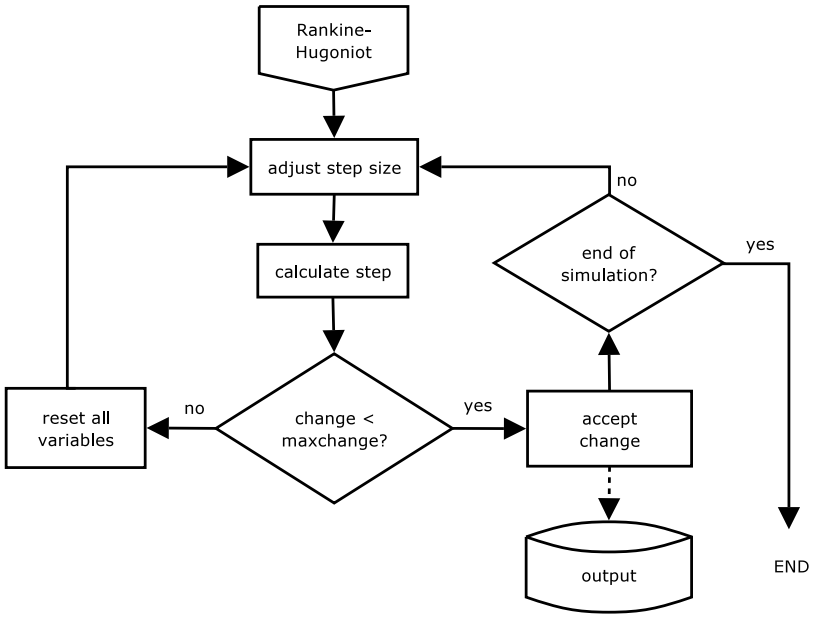

Figure 3.2: Flow chart for the adaptive step size control. The acceptable value for the maximum change is a program parameter

spheric processes which are not included in the simulation. The program aborts with an error message if it detects a NaN or reaches a maximum depth or a maximum number of steps (to avoid endless loops while simulating larger grids). The change for the gas dynamic variables (density, bulk velocity, temperature of ion and electron component, electron to ion ratio and energy loss rate) is calculated relative to the last time step. For the ion fraction it is defined as the absolute difference to the last time step. This is necessary to avoid problems with very small ion abundances at the edge of numerical precision. No distinction is made between abundances of different elements. If e.g. the maximum change allowed is 0.1 than $\Delta n_{HI} = 0.11$ will force the program to redo the step with a smaller step size the same way as e.g. $\Delta n_{CoXXVI} = 0.11$. This is necessary to obtain a good accuracy for the line data of every element. After each step, accepted or discarded, the algorithm interpolates linearly and sets the new step size in such a way that the predicted change will be half the maximum. For only slowly varying quantities this assures that after the first the next step is most likely accepted as well and computing time is not wasted. There is another programme parameter which controls the minimum step size. Under no circumstances a step can be smaller than this in order to prevent situations where the continuum treatment is no longer possible.

3.1.3 Data sources

The module for microscopic physics needs atomic input data. All parts which are handled by the CHIANTI software, the excitation/deexcitation calculations, of course use the CHIANTI database (Young et al. 2003; Dere et al. 1997). The dielectronic recombination coefficients are taken from Mazzotta et al. (1998). They take data from various sources (see their paper and references therein) and fit them with a single formula with tabulated coefficients. For the radiative recombination and the ionisation (collisional and auto-ionisation) rate I use a code from D.A. Verner, which is available in electronic form on the web[1]. The data sources for the radiative recombination coefficients are given in table 3.1. The ionisation data is taken from Arnaud and Raymond (1992) for Fe, from Arnaud and

[1] http://www.pa.uky.edu/∼verner/fortran.html

H-like, He-like, Li-like, Na-like	Verner and Ferland (1996)
Other ions of C, N, O, Ne	Pequignot et al. (1991) refitted by Verner and Ferland (1996) formula to ensure correct asymptotes
Fe XVII-XXIII	Arnaud and Raymond (1992)
Fe I-XV	refitted by Verner and Ferland (1996) formula to ensure correct asymptotes
Other ions of Mg, Si, S, Ar, Ca, Fe, Ni	Shull and van Steenberg (1982)
Other ions of Na, Al	Landini and Monsignori Fossi (1990)
Other ions of F, P, Cl, K, Ti, Cr, Mn, Co (excluding Ti I-II, Cr I-IV, Mn I-V, Co I)	Landini and Monsignori Fossi (1991)
All other species	interpolations of the power-law fits by Verner

Table 3.1: Articles with data used by the Verner recombination code

Rothenflug (1985) for H, He, C, N, O, Ne, Na, Mg, Al, Si, S, Ar, Ca, Ni (with some corrections described in Verner and Iakovlev (1990)) and from interpolation/extrapolation by Verner for other elements. The code is supplied in Fortran language. I translated it to C with the f2c converter, because C matches the IDL portable calling convention for calling shared objects without large modifications. Voronov (1997) published a newer data compilation, but according to Mazzotta et al. (1998) it suffers from a misprint in one of its sources which is only partially corrected. This would give rates which are nearly a factor of 2 wrong.
The Verner codes work from H ($Z = 1$, Z is the electric charge of the nucleus) up to Zn ($Z = 30$), but for the dielectronic recombination Mazzotta et al. (1998) the coefficients are only published up to Ni ($Z = 28$)

3.2 Verification

Errors in programming inevitably occur and extensive testing is necessary to verify that the simulation reproduces the physics correctly.

3.2.1 Gas dynamics

If no energy is lost due to radiation and the flow is subsonic the equations from section 2.1 predict a steady flow. I ran the hydrodynamic module with numerous input parameters over a wide range and it always responded as expected. In the post shock zone there are never supersonic velocities because the material is decelerated in the initial shock. The module issues an error if started with supersonic gas velocities.
Furthermore, the heat transfer between the two components of the gas, ions and electrons is tested. Under certain simplifying assumptions (although maybe unphysical) I can derive an analytic solution how the temperature depends on depth or time. The following example is done for a pure, completely ionised hydrogen gas. The ionisation state is set constant because otherwise a calculation of the microscopic physics would be necessary as well. In equation (2.31) the abundance of hydrogen $\xi_H = 1$ and the ionisation $x_H^1 = 1$ are replaced by their numerical values and the equation now reads

$$\omega_{ei} = \frac{3}{2} k \frac{\Lambda}{252} \frac{T_{ion} - T_{elec}}{T_{elec}^{3/2}} \tag{3.1}$$

Density n and bulk velocity u are constant and because of that the Coulomb-logarithm Λ from equation (2.32) is constant, too. Placing all this

in equation (2.33) now results in an easily solvable differential equation:

$$v\frac{3}{2}k\frac{\partial T_{ion}}{\partial z} = -n\frac{3}{2}k\frac{\Lambda}{252}\frac{T_{ion}}{T_{elec}^{3/2}} + n\frac{3}{2}k\frac{\Lambda}{252}\frac{1}{\sqrt{T_{elec}}} \tag{3.2}$$

The homogeneous part is solved with an exponential ansatz and the complete solution is derived by varying the constant. This solution is

$$T_{ion}(z) = A_0 \exp(-x\frac{n\Lambda}{v252T_{elec}^{3/2}}) + T_{elec} \tag{3.3}$$

A_0 is set by the initial conditions. In figure 3.3 a test run is plotted. Instead of the space x the x-axis shows the time from $t = \frac{v}{x}$ for a plasma with $v = 50$ km/s and mass density $\rho = 10^{-12}$ g/cm^3. The temperature slowly reaches the constant electron temperature from below. For a large temperature difference more heat is transferred and the ion temperature rises faster. As the ion temperature rises, the exchange gets slower. Simulation and analytic solution from equation (3.3) coincide. This shows that the code models the heat transfer correctly. Calculations for constant ion temperature give a picture which is qualitatively similar, but because the dependence of ω_{ei} and Λ is more complicated I do not present an analytical solution here. If both temperatures are free, they converge against their mean value because electrons and ions have the same number of degrees of freedom so they get the same energy per Kelvin according to equation 2.7. These tests give me confidence that the hydrodynamics module works as expected.

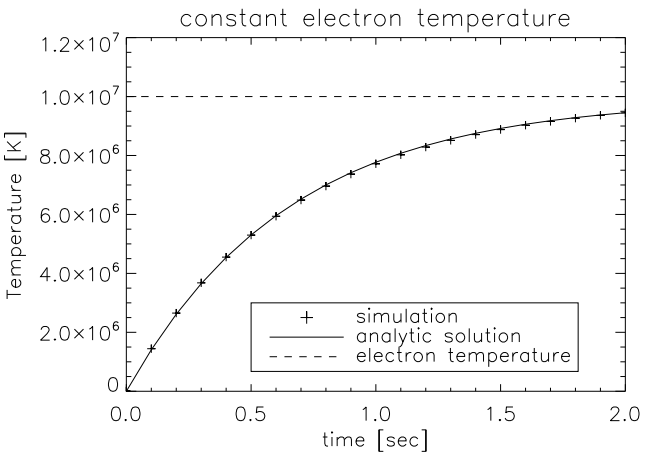

Figure 3.3: Simulation and analytic solution for a situation of gas with different electron and ion temperature, velocity $v = 50$ km/s and mass density $\rho = 10^{-12}$ g/cm^3

3.2.2 Ionisation/Recombination

My choice of data is very similar to that of Mazzotta et al. (1998). To check my implementation I took ionisation equilibria from three different sources. First the published data from Mazzotta et al. (1998), second the ionisation equilibrium calculated from the matrix equation 2.55 and third the microscopic physics module of the simulation program started with any ionisation state and simulating a long time until everything relaxes to the equilibrium state. The second and the third check internal consistency and stability of the numerical algorithm for ionisation and recombination. The resulting ionisation equilibria are equal to a precision far below 1%. Mostly they also match the Mazzotta et al. (1998) values. In figure 3.4 and figure 3.5 the ionisation fractions for the elements with the largest differences are shown. Mazzotta et al. (1998) uses data without the corrections from Verner and Iakovlev (1990) so I expect deviations on at least some elements. These checks

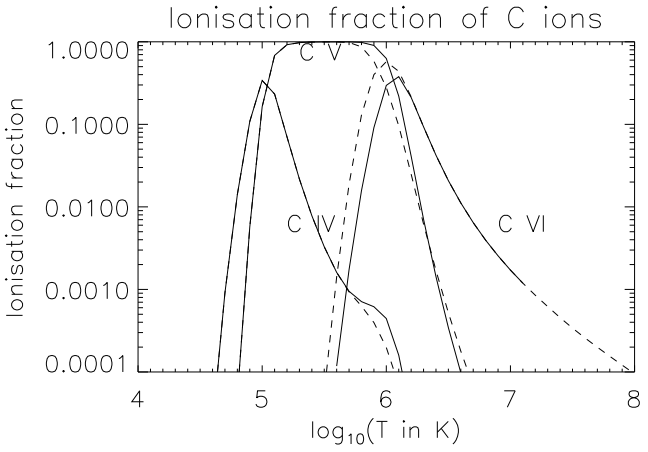

Figure 3.4: Ionisation fractions for selected ions of C; solid lines: Mazzotta et al. (1998), dashed lines: simulation

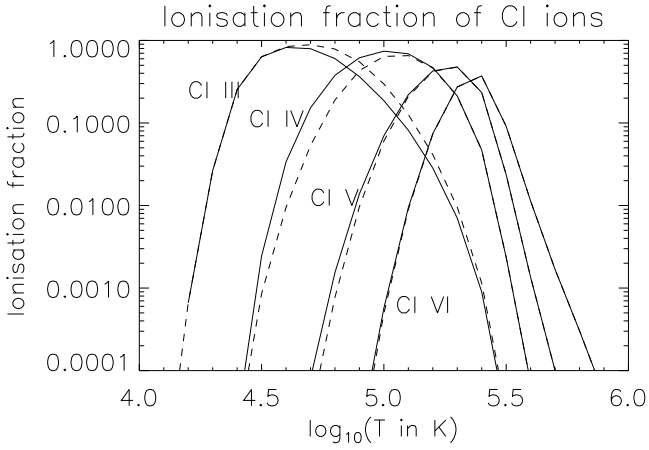

Figure 3.5: Same as in 3.4 for Cl

show that the rates for ionisation and deexcitation produce the correct equilibria. What is still missing is a proof of the correct behaviour in time. Unfortunately, there are no laboratory measurements under comparable circumstances published. It is difficult to set up a collisionally dominated plasma and measurements are often done by lasers which introduce important processes of stimulated emission (see for example Burgess et al. 1980). I did not want to write another simulation just to find that for some reason the laboratory values depend on other uncontrollable parameters like the purification of the gas used, so an analytic solution for the time dependence of the ionisation fraction of pure hydrogen was used. This has only one electron and therefore only one ionised state which makes the solution easy for a gas of constant temperature and proton density n. Writing down the rate equation (2.54) and realising that the electron density n_e equals the density of ionised hydrogen n_2 leads to (a dot denotes a time derivative)

$$\begin{aligned}\dot{n_2} &= n_1 n_e R_{1\to 2} - n_2 n_e R_{2\to 1} \\ &= n_1 n_2 R_{1\to 2} - n_2^2 R_{2\to 1}\end{aligned} \tag{3.4}$$

With the normalisation condition $n_1 + n_2 = n$ this further simplifies to a differential equation of just one parameter (n_2):

$$\dot{n_2} = (n - n_2) n_2 R_{1\to 2} - n_2^2 R_{2\to 1} \tag{3.5}$$

The stationary equilibrium is

$$n_2(t=\infty) = n \cdot \frac{R_{1\to 2}}{R_{1\to 2} + R_{2\to 1}} \tag{3.6}$$

DGL (3.5) is of Bernoulli's type. So the substitution with $z = n_2^{-1}$ linearises it.

$$-\dot{z} = n R_{1\to 2} z - (R_{1\to 2} + R_{2\to 1})$$

$z(t) = A\exp(-nR_{1\to 2}t)$ solves the homogeneous part and variation of the constant gives a special solution of the inhomogeneous equation: $z(t) = \frac{R_{1\to 2}+R_{2\to 1}}{nR_{1\to 2}}$. The general solution is then the sum of both.

$$z(t) = \frac{R_{1\to 2} + R_{2\to 1}}{nR_{1\to 2}} + A\exp(-nR_{1\to 2}t) \tag{3.7}$$

Here A is a constant set by the initial condition. Now I return to the original problem in 3.5 and define the typical relaxation time scale $\tau^{-1} = nR_{1\to 2}$. Furthermore, the whole equation is divided by the density n to obtain the ion fractions x.

$$\begin{aligned}x_2(t) &= \frac{x_2(\infty)}{1 + \left(\frac{x_2(\infty)}{x_2(0)} - 1\right)\exp(-t/\tau)} \\ &= \frac{x_2(0)x_2(\infty)}{x_2(0) - (x_2(0) - x_2(\infty))\exp(-t/\tau)}\end{aligned} \tag{3.8}$$

Several different situations can be modeled and compared to this formula. A first test starts at any temperature with neutral hydrogen. Equation (3.4) shows that nothing should happen because there are no initial electrons and so no reactions take place. The simulation gives a static solution as well, but this is an unphysical question, because in reality at least a few atoms are always in the state H II and anyway there is a small chance to ionise one of the partners in a neutral-neutral collision. In real stellar plasma the contribution of this process is negligible and is not implemented in the code. More interesting is the situation for starting with a completely ionised plasma. At relatively low temperatures parts of it recombine and the fraction of $x_1 = 1 - x_2 = n_{HI}/n_H$ converges to its equilibrium value. Figure 3.6 shows a nearly perfect

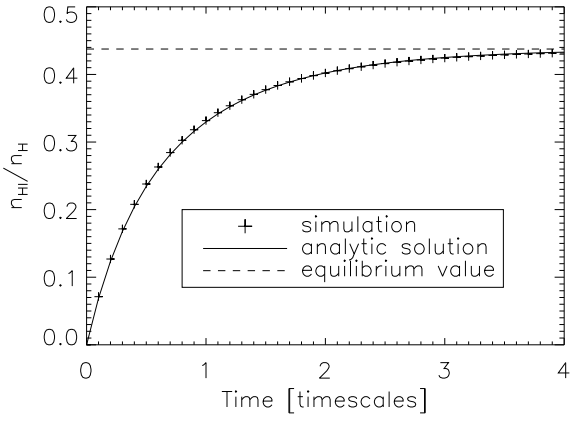

Figure 3.6: Time evolution of the HI fraction in a pure hydrogen gas. The analytic solution is calculated with equation 3.8

match between theory and simulation. Further tests for other elements show a behaviour that is qualitatively similar, but analytic solutions for heavy elements are hard to find. This is the last step for the verification of the microscopic physics module: The ion fractions converge towards the correct values in the correct time.

3.3 Accuracy and program parameters

Numerical errors are introduced in different ways. I will discuss sources of errors from the atomic data to the final analysis of simulation results. The hydrodynamic calculations only require a few very well known fundamental constants like Boltzmann's constant k and the masses of atoms or electrons. The uncertainty in these data is negligible. The situation is more complicated for the microscopic physics. Here large sets of atomic data are needed: Coefficients for collisional ionisation and recombination and all the data in the CHIANTI database for excitation/de-excitation calculations which form the emission lines. Several authors stress the importance to use accurate atomic data (Brickhouse 1999; Kaastra 1998), but laboratory measurements exist only rarely. del Zanna (2002) compares different plasma codes in the X-ray region and concludes that CHIANTI in general works as well as others. The accuracy of single line data depends on the particular transition in question and ranges from better then 1% up to a factor of maybe two (Landi et al. 2002). New and more accurate data is published frequently. I did the simulation with CHIANTI v.4.2 (Young et al. 2003) and the analysis of line ratios with the new version CHIANTI v.5.0 (Landi in press).
The overall energy loss due to radiation is the sum of bound-bound, free-bound, and free-free processes. The contribution of bound-bound emission is typically larger than the others by one or two orders of magnitude. So the error is basically given by the line emission. Each line has a different accuracy and its importance depends on the temperature, which makes it is difficult to judge the total error. CHIANTI provides a routine (bb_rad_loss.pro) to calculate the energy loss via line emission. It uses the approximate method of Mewe et al. (1986) with an accuracy ~ 10 %, but this is numerically unstable if used out of equilibrium which is necessary in this simulation. The simulation uses more detailed CHIANTI methods, which should result in more exact results, that is the error should be less than 10 %.
In section 3.1.2 the errors introduced by separating the equations for gas dynamics and microscopic processes are already discussed. Two program parameters adjust this. Any parameter is allowed to change only by some specified maximum fraction. The smaller this value the more steps are done and the smaller the error, but also the more time is needed. In the beginning right behind the initial shock and at the end of the cooling zone lots of ionisations and recombinations occur. A small maximum change leads to very small step sizes in these regions, but they emit only a few photons and their accuracy is not as important as that of the large regions in the middle of the shock, because all observational quantities like line ratios or intensities are integral quantities over the entire shock region. Figure 3.7 showns how the simulated shock depth depends on the minimum step size (left) for typ-

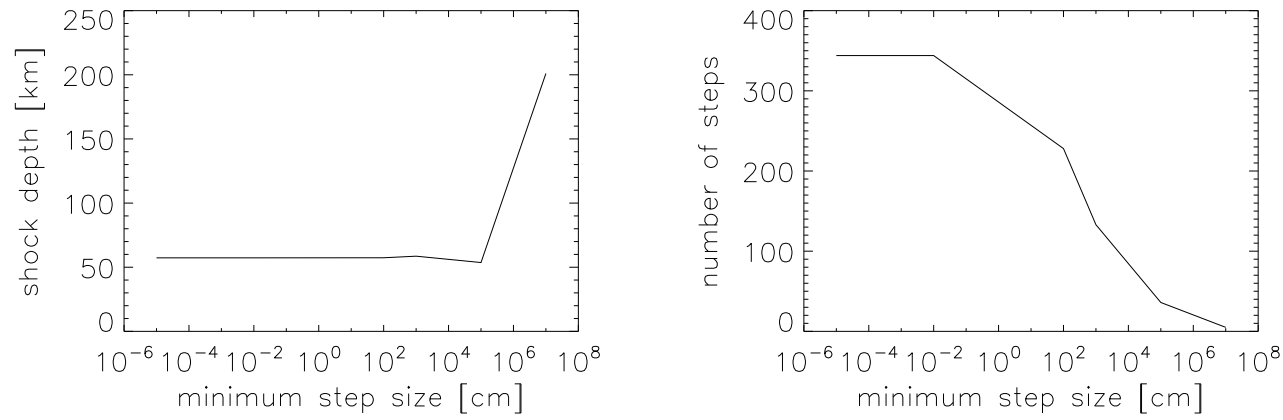

Figure 3.7: The dependence of the depth of a shock (left) and the number of steps (right) on the minimum steps size

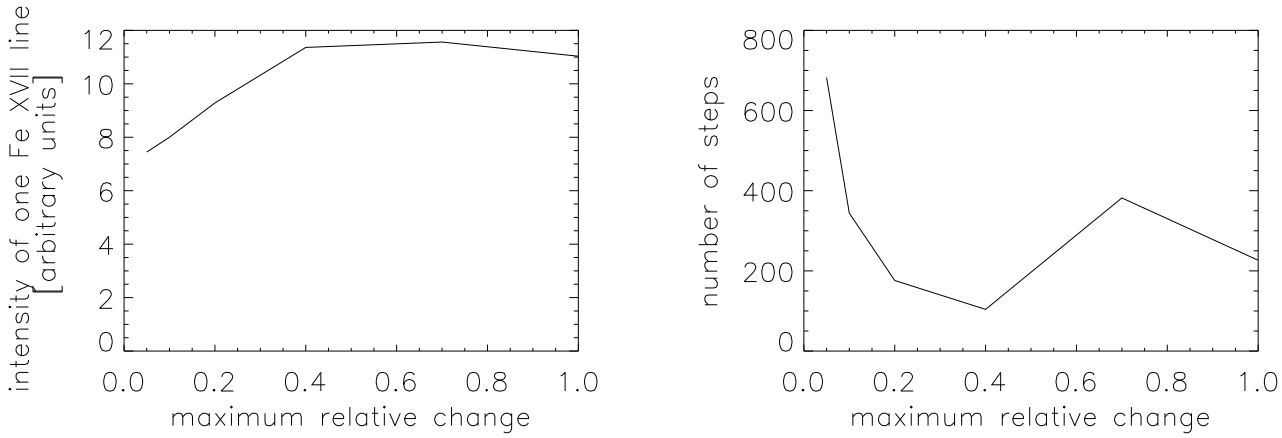

Figure 3.8: The dependence of the intensity of a Fe XVII line (left) and the number of steps (right) on maximum change per step

ical shock parameters and a maximum change of 10%. For small values of the minimum step size the resulting depth is the same, for very large steps (about 10^5 cm) the results are different. With a minimum step size of 10^7 cm the whole cooling region is simulated in only two steps. Obviously these results cannot be very physical. Other quantities like line intensities behave similarly. In the right hand plot of figure 3.7 the number of steps, which is a good measure for the computing time, is shown. Increasing the minimum step size makes the execution faster. Choosing a minimum step size conservatively I take 10^2 cm. This so small that it should give good results, but saves already about one third of the time compared to setting no minimum size. The accuracy is then basically set by the maximum relative change per step that controls how fast changes from gas dynamics effect the microscopic physics and the other way round. In figure 3.8 the intensity of one line of Fe XVII (at 15.02 Å) is shown. Figure 3.9 explains where the difference of the intensity in figure 3.8 arises. In calculations with larger changes per step the step size is larger. In the dash-dotted and dashed lines the sharp edges between the steps are clearly visible. The large steps mean that the ion does not recombine fast enough. The intensity of a line is proportional to

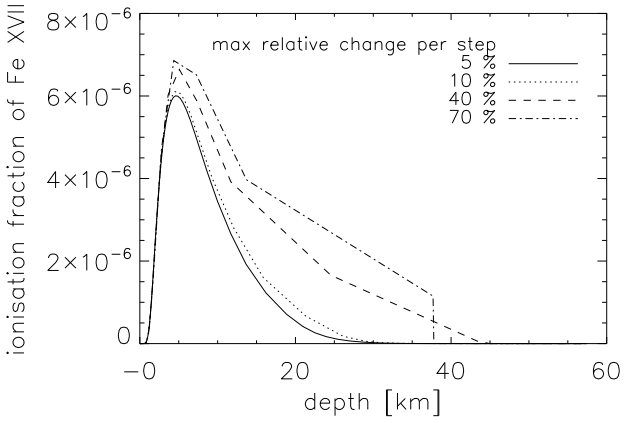

Figure 3.9: Ionisation fraction of Fe XVII calculated with different accuracy

the ion fraction multiplied by the density which is nearly constant in the regions which are of interest here. So the calculated line intensity is too large. For small changes per step the curve looks smooth as expected for a freely flowing gas. This indicates that the model is close to a possible physical situation. Maximum changes above 40% are for illustrative purposes only: The linear interpolation that predicts the next step size is no longer a good approximation and the number of steps actually rises again (right part of 3.8) because the next step size begins to fluctuate widely.
For smaller maximum changes the number of steps rises fast (3.8 right panel), but the physical parameters do not reach a constant value.

Smaller changes per step deliver different (and presumably more accurate) results. A compromise is needed between the required accuracy and the computation time available. I chose a maximum relative change per step of 5%, in most cases it is smaller because the program sets the step size in a way that a change of 2.5% is expected in order to make the next step pass the accuracy test with a high chance.
The integration of the single ODEs within the modules is done by the built-in IDL function 'lsode' to local relative tolerance of 10^{-7}. It is difficult to combine all error estimates to a global error because they contribute differently at different times and positions. Some errors are self-regulating, if e.g. in one time step the ionisation state of any atom is calculated too high for any reason in the next time step there will be a stronger recombination and it drops again. This is the best case, usually errors propagate and effect other variables as well. It is important to keep this point in mind and analyse which variables are more stable than others. Lines formed in the central cooling region are presumably more accurate than lines from ions which occur only as intermediate step in the ionisation process right behind the shock front because here changes occur on the same scale as the step size. Comparing line ratios instead of absolute fluxes has the advantage that errors of the total intensity divide out. If, for example, lines are formed in the same temperature region then they will originate in the same volume of gas and their ratio is independent of the volume emission measure.

Chapter 4

Results

In this section I describe and discuss the results of the shock simulation. In section 4.1 the structure of the shocks is discussed. This includes the temperature, density and ionisation profiles and allows to check some assumptions made earlier about the geometry and the thermal heat flux. It is also shown that the shock structure basically depends only on the density and velocity of the infalling gas. The second section 4.2 deals with the emission from the shock and describes how to distinguish different scenarios by analysing line ratios. For the example of Ne IX it is shown in great detail in which region of the shock several lines are formed. These results are applied to observations of the CTTS TW Hydrae in section 4.3, the infall velocity and density are identified and further shock characteristics (filling factor and mass accretion rate) are calculated. In section 4.4 I try to fit my simulation to data from BP Tau, but no satisfying match is achieved.

4.1 Model parameters

The shock structure cannot be observed directly because it is not spatially resolved. Accordingly there is only the simulation to guide our understanding about e.g. temperature, density and ionisation profiles.
It has to be remembered that some simplifications are made (see section 2.1.3), especially that the simulation has no explicit time dependence and no turbulent flux.
The shock itself occupies a very thin layer (see section 2.1.5). The temperature of the ion component rises at the shock front and energy is transferred to the electrons so they heat up as well. In the following figures I will use a shock with typical behaviour as an example. It is calculated with values for v_0 similar to typical free-fall velocities for CTTS and densities n_0 motivated by X-ray measurements (Stelzer and Schmitt 2004). In the pre-shock region ions and electrons have time to equalise their temperatures, the value is taken from photoionisation calculations by Calvet and Gullbring (1998). The input parameters are summarised in table 4.1. Figure 4.1 shows a sketch illustrating the accretion geometry and the nomenclature I use.

4.1.1 Temperature and density profiles

Figure 4.2 shows simulated temperature and the density profiles. The temperature shown in the plot is the temperature of the ion component. Directly behind the shock front, defined as depth 0 km, it cools down fast because it transfers energy to the electrons by collisions. After a few kilometers both components have nearly identical temperatures and henceforth there is basically only radiative heat loss. This is the post-shock zone where the radiation originates, which is analysed in this thesis. During the process of cooling the density rises and because of momentum conservation the gas slows down simultaneously (equation 2.20). The emissivity of a line is proportional to the number of electrons and to the number of ions in question, for constant ionisation fractions this means that it is about proportional to the square of the density. As more energy is lost from the system the density increases and it follows that the energy loss rate

parameter	symbol	value
infall velocity	v_0	400 km/s
infall density	n_0	10^{12} cm^{-3}
ion temperature	T_{ion_0}	20000 K
electron temperature	T_{elec_0}	20000 K
initial ionisation states		Arnaud and Rothenflug (1985)

Table 4.1: Initial pre-shock conditions for a 'typical' shock discussed in the following sections

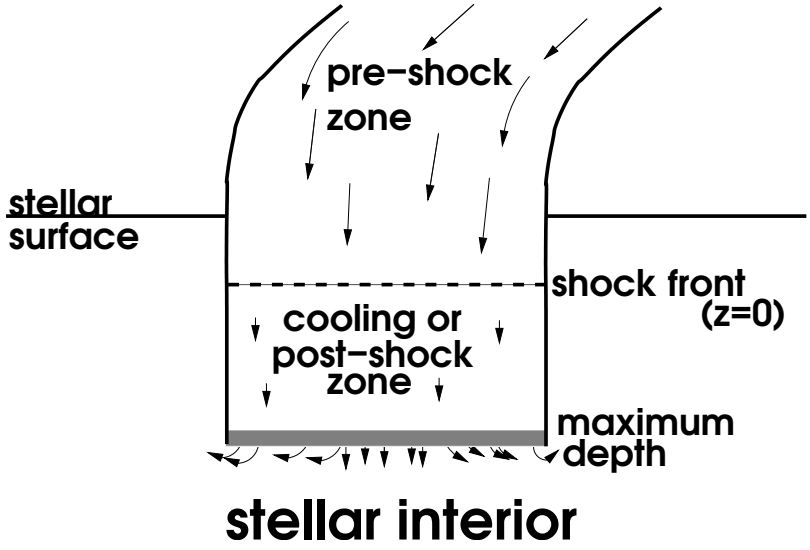

Figure 4.1: Illustration showing the different zones in the shock. Arrows show the particle flux.

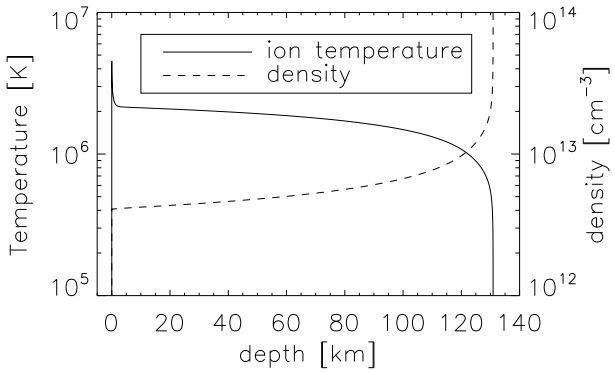

Figure 4.2: Temperature and density profiles for a shock calculated with the initial conditions from table 4.1

does as well. So the gas cools down very fast in the end. The simulation stops when the temperature drops below 12000 K ('maximum depth'), where the calculation is not valid any longer because the energy that is transported from the central region of the star to its surface becomes important and also the optical depth increases, consequently radiation transfer has to be modelled. Both problems are not included in this simulation. In this region the accreted material mixes with the stellar atmosphere.

The typical shock reaches about 130 km depth, which is much smaller than a stellar radius. In this way the simplifying assumption of a planar star surface in section 2.1.3 is justified a posteriori. These calculations agree qualitatively with Lamzin (1998) and Calvet and Gullbring (1998) and lie quantitatively between their results.

The region where the electron temperature differs significantly from the ion temperature is much

smaller then the maximum depth. A two fluid treatment is not necessary for most parts of the shock, which was already assumed in previous calculations (Lamzin 1998; Calvet and Gullbring 1998). In figure 4.3 the electron and the ion temperature are plotted in comparison. At the shock front the electrons stay relatively cool because they are only compressed adiabatically. The energy flows from the ions to the electrons and already in a depth of 2 km their temperatures are nearly equal at the order of two million Kelvin. Electrons and ions have the same number of kinetic degrees of freedom and therefore get the same thermal energy per particle. Their number density is similar and so the temperature equalises at about half the initial four million degrees.

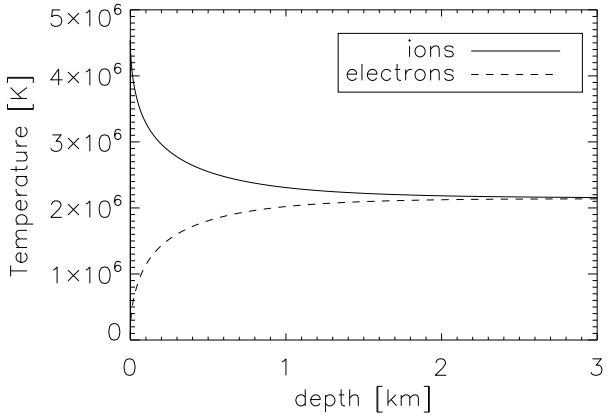

Figure 4.3: Ion and electron temperatures in the upper post-shock region for a shock calculated with the initial conditions from table 4.1

4.1.2 Ionisation states

The simulation starts with the ionisation equilibrium for T_{ion} from Arnaud and Rothenflug (1985). In fact, this may underestimate the degree of ionisation, because the shock is very hot and emits hard radiation which photoionises the infalling gas. Calvet and Gullbring (1998) calculate this pre-shock stage by a photoionisation code using their shock emission as an input and find that hydrogen is ionised completely at least 100 km above the stellar surface.
Moreover we know that the large scale structure of the infalling matter column cannot be described in a one dimensional model. In strict 1D approximation all emission gets absorbed by the matter in the (infinite) infalling column. The geometrical configuration of the funnel flow is still unknown and so is the proportion of emitted photons ionising atoms in the pre-shock accretion flow. To solve this problem by a simulation including non-equilibrium effects requires vast computing resources because in principle it has to be done iteratively. Fortunately, the dependence of the calculated shock properties on the initial ionisation state is only weak and any state which provides a reasonable number of electrons to start further ionisation processes will do. The temperature behind the shock is several orders of magnitude larger than that of the infalling gas, therefore the remaining atoms are ionised to high stages very quickly. This stops when the collisional ionisation equilibrium corresponding to the local temperature is reached. The ionisation cross section depends on the element, but generally the situation is close to equilibrium after a few km which is short compared to the maximum depth of the shock. The required ionisation energy cools the gas only slightly. Stripping O I to O VII needs about 400 eV. This is comparable to the kinetic energy of a single particle before the shock, but elements which are easier to ionise like hydrogen and helium are by far more abundant, so the energy loss is much smaller on average. In the main cooling zone the ionisation state stays close to the local collisional equilibrium state. When the temperature drops, recombinations occur until the simulation stops. In real stars the recombinations go on until stable photospheric conditions are reached.

As an example figure 4.4 shows how the ionisation depends on depth. The charge of the most abundant iron ion is plotted. Initially this is Fe III (charge 2) and in the hot environment behind the shock it quickly ionises to Fe XV. Then the gas cools down and the ions recombine slowly maintaining the ionisation equilibrium. At ∼120 km the temperatrue drops so fast (see figure 4.2) that

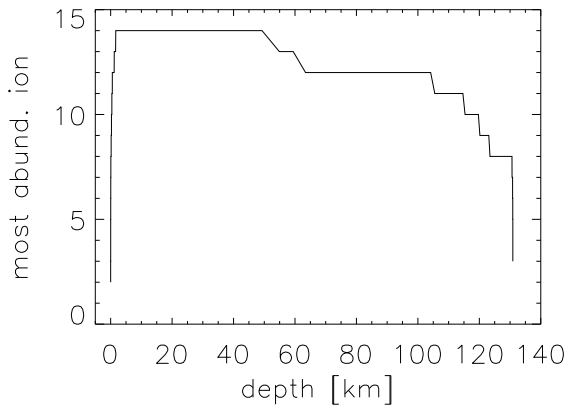

Figure 4.4: Charge of the most abundant iron ion in different depth in a shock calculated with the initial conditions from table 4.1. Iron ionises fast and then slowly recombines while the gas cools.

the recombinations cannot keep step and the ions drop out of equilibrium. A more detailed discussion for the example of neon can be found in section 4.2.1

Several simulations were performed to investigate the influence of the initial ionisation stages. Virtually no emission is produced by the initial ions, because the ionisation processes happen very fast. The main influence of the initial ionisation state is that slightly higher temperatures are reached if the ionisation degree is higher and so the cooling time is longer. Therefore, the integrated intensity of all lines which originate in the main cooling zone between 10 and 120 km depth is slightly higher, but the first few ionisations do not need much energy so the effect is only marginal. Simulations starting with the same gas temperature but different ionisations show that line ratios are nearly equal and strong lines are only affected within a few percent. Still it is possible that the slightly higher temperature just builds up, e.g. Ne X for a short time where usually Ne IX is the highest ionisation state. This induces the presence of additional weak Ne X lines. If the ionisation is lower than assumed in table 4.1, lines formed in the hot parts of the plasma are weaker.

4.1.3 Influence of the initial temperature

The initial temperature is only important through its influence on the initial ionisation state. Using the equations (2.6) and (2.7) the thermal energy per particle and its bulk kinetic energy can be compared. The thermal energy is about a few eV, the kinetic energy a few hundred of eV mostly converted into heat by the shock. Equation (2.31) shows that the energy transfer from the hotter to the cooler component is fastest where the temperature difference is largest. Compared to the $\approx 10^6$ K of the ion gas just behind the shock front a difference in electron temperature of 10^3 K is insignificant.

4.1.4 Influence of density and infall velocity

Using the ionisation state and the temperatures from table 4.1 I calculated a grid of simulations with the parameters velocity ranging from 200 km/s to 600 km/s in steps of 25 km/s and densities between 10^{10} cm^{-3} and 10^{14} cm^{-3} with 13 points equally spaced on a logarithmic scale. The infall velocity and the density are the physically most interesting parameters. In sections 4.3 and 4.4 only these two are varied to fit observations to the simulation. They have a strong impact on the characteristic properties of a shock. The maximum post-shock temperature of the ion component T_1, for example, depends quadratically on the infall velocity v_0, but not on the density. This can be seen directly by transforming equation (2.5):

$$T_1 \sim \frac{P_1}{n_1} \sim \frac{n_0 v_0^2}{n_1} \sim v_1 u_0 \sim v_0^2 \qquad (4.1)$$

In the second step P_1 is expressed with equation (2.26) neglecting the initial pressure P_0, in the third step I use the particle conservation law in the form (2.22). In the last the combined equations (2.26) and (2.27) again taking $P_0 = 0$. Figure 4.5 shows contour lines of constant maximum ion temperature. They are parallel to lines of constant infall velocities, only for

very small densities the approximation above is no longer strictly valid and the lines curve. They are spaced with constant temperature differences and their difference in velocity space decreases according to (4.1). A second example for a shock

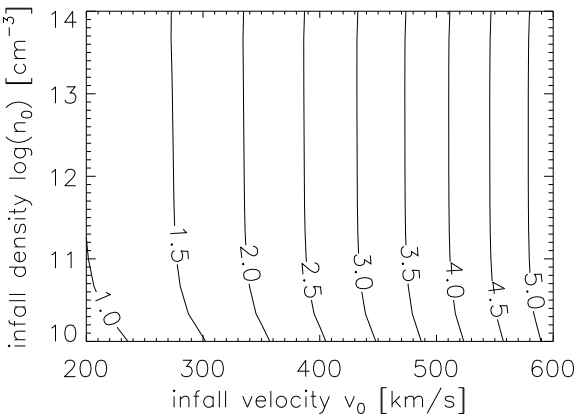

Figure 4.5: The lines mark parameters with constant ion temperature behind the shock in units of 10^6 K.

property that varies depending on the infall density and velocity is the length of the cooling zone, which will be discussed in the next setion.

4.1.5 Depth of shock

In figure 4.2 the temperature and density profiles for a typical shock are plotted. All calculated shocks exhibit the same qualitative behaviour, but large quantitative differences, especially the length of the cooling zone varies over 3 orders of magnitude. A higher infall velocity leads to a deeper shock because the material reaches higher temperatures and consequently needs longer to cool down, so it flows for longer times and reaches deeper regions. A second correlation is more surprising: Lower infall densities result in shocks with a larger spacial extent. Gas emits energy roughly proportional to the square of the density, therefore lowering the density will increase the time the gas needs to cool down to stellar temperatures. Figure 4.6 shows contour lines of constant maximum depth, which are plotted a constant factor apart. They appear to be evenly spaced on linear scales, which proves exponential dependence of the depth on the infall density and velocity. High velocities and small densities im-

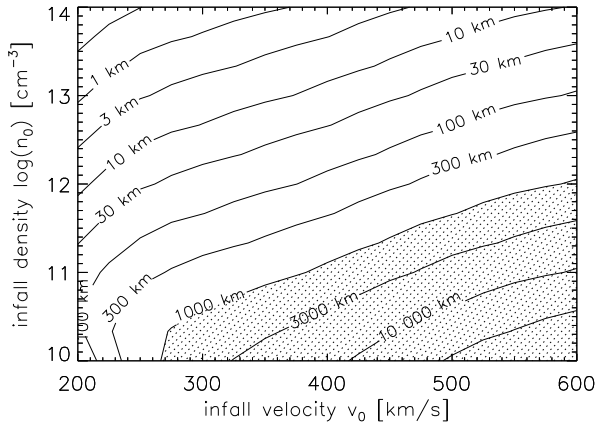

Figure 4.6: The length of the cooling zone ('maximum depth') dependent on the logarithm of the infall density $\log(n_0)$ and the infall velocity v_0: The length of the cooling region is labeled. The dotted area marks regions where the deeper parts of the simulated shock are not included in line emissivity calculations.

ply a long time needed to cool the gas down.
In the hydrodynamics approach used in this simulation there is no direct influence of the star on the gas, therefore caution has to be applied when interpreting these results, especially for thin infalling gases. After the shock has occurred there is essentially free-flow during cooling. If the gas has a high ram pressure this picture works well. The surrounding atmosphere is pushed away and it mixes with the accreted material only after cooling. For thin gases the ram pressure is much lower and additionally they need more time to cool down. They may be strong enough to push the thin upper atmosphere, but the density of a star increases with depth. So in deeper layers the approximation of a free flowing gas is no longer valid and the whole calculation breaks down. The depth where this happens depends, of course, also on the parameters of the star. Right behind the shock the conditions will be as predicted and data for lines originating in this region can be analysed as usual, but emission from lay-

ers below a few hundred km will be affected.
The shock front forms when its ram pressure equals roughly the gas pressure of the stellar atmosphere. The ram pressure is

$$p_{ram} = \rho v_0^2 \tag{4.2}$$

After passing through the shock front the shock pressure actually decreases because the gas decelerates to about $\frac{v_0}{4}$ (equation 2.26 and 2.27, neglecting the initial pressure P_0). This is not balanced by the increase of thermodynamic pressure according to equation (2.5) although the temperature rises significantly. This means that the shock gas will have a pressure comparable to or even lower that the surrounding medium. The deeper it penetrates into the star the larger the pressure of the surrounding atmosphere becomes. To estimate the orders of magnitude of pressure I use an atmospheric model from the *PHOENIX* programme. *PHOENIX* is a general purpose stellar atmospheric modelling code which uses more than 500 million lines for its radiation transport calculations. I use here a density profile from AMES-cond-v2.6 with effective temperature $T_{\rm eff}$ = 4000 K, surface gravity $\log g$ = 4.0 and solar metalicity (Brott and Hauschildt (2005) based on Allard et al. (2001)) to compare realistic atmospheric pressures to the shock ram pressure. The stellar parameters chosen resemble those of typical CTTS (see section 1). Inserting them into equation (4.2) I obtain $p_{ram} \approx 3500 \frac{n_0}{10^{12}\mathrm{cm}^{-3}} \left(\frac{v_0}{400\ \mathrm{km/s}}\right)$ dyn. In figure 4.7 the pressure in the atmosphere is shown. The origin of the stellar depth has been set for this plot where the stellar pressure equals 100 dyn. For the standard shock from table 4.1 the ram pressure equals the atmospheric pressure at about 650 km, figure 4.6 shows that the cooling length is about 100 km. The upper black bar in figure 4.7 illustrates this situation. The bar starts where the ram pressure equals the thermodynamic pressure of the surrounding atmosphere and it extends of 100 km. The stellar pressure at the end of the cooling zone (at 650 km+100 km=750 km) differs from that at the shock front roughly by a factor of two. For lower densities and higher infall velocities

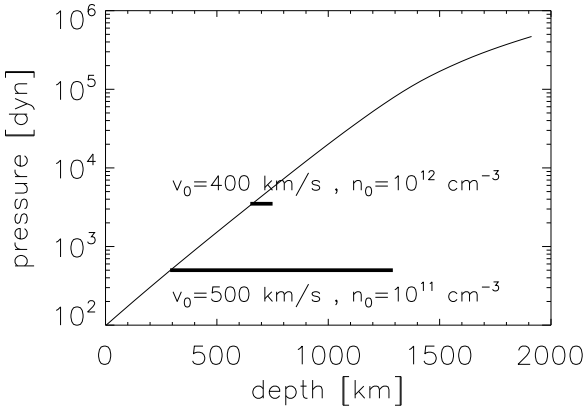

Figure 4.7: Pressure in a stellar atmosphere of a star with $T_{\rm eff}$ = 4000 K, logg=4.0 and solar metalicity from *PHOENIX* (thin solid line). The bars and labels illustrate two examples for the position of a shock in the atmosphere (see text).

like e.g. $n_0 = 10^{11}$ cm^{-3} and $v_0 = 500$ km/s this ratio reaches quickly two orders of magnitude (lower black bar in figure 4.7). In this case it is not justified to use this shock model. The pressure rises exponentially, so independent of the starting point only shocks with small cooling length can be described by the hydrodynamic modelling used here. For larger stars, i.e. smaller log(g), the pressure does not rise as fast as in figure 4.7, but still the pressure difference between the shock front and the maximum depth is at least an order of magnitude if the shock extends more than 1000 km. Because of that all line fluxes are integrated between the shock front and the maximum depth or 1000 km whichever is less.

4.1.6 Thermal conductivity

Thermal conduction tends to smooth out temperature gradients. It is not included in the simulation (see section 2.1.3), still the temperature gradients in the models now allow to estimate its importance. It is possible to derive the thermal conduction heat flux from kinetic gas theory but I use the formula from Spitzer (1965,chapter 5.5)

here.

$$F_{cond} = \kappa_0 T^{5/2} \frac{dT}{dz} \tag{4.3}$$

Here $\kappa_0 = 2 \cdot 10^{-4} \frac{\delta_T}{\Lambda} \frac{\text{erg K}^{7/2}}{\text{s cm}}$ is the coefficient of thermal conductivity and δ_T is a correction factor to relate real gases to ideal behaviour. For hydrogen δ_T is of the order 0.1. I now compare the thermal heat flux according to equation (4.3) to the energy flux by the bulk motion which transports heat and bulk kinetic energy. For a typical shock their ratio is shown in figure 4.8. It is

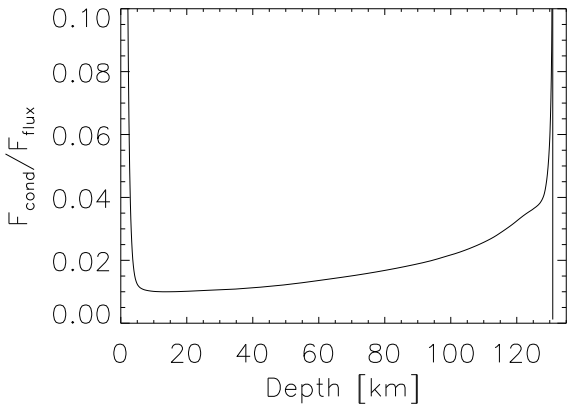

Figure 4.8: Ratio between thermal heat conduction F_{cond} and energy flux by bulk motion F_{flux} for a typical shock (table 4.1)

large right behind the front, reaches a minimum and increases slowly again towards the maximum depth. The thermal flux is important close to the shock front because it transports the thermal energy produced there upstream in the preshock zone and heats the inflowing gas to the 20.000 K assumed in table 4.1. It will distribute some energy downstream of the shock front, too, but the main part of the cooling zone is affected only marginally. In the end the temperature gradient again becomes much steeper, but in this region the gas is quite cool already and therefore the absolute magnitude of F_{cond} small according to equation 4.3.

The energy flux due to bulk motion (the two left terms in equation 2.13) is proportional to the number density. Accordingly the thermal heat conduction from equation (4.3) is more important for low density scenarios, but apart from lowest density cases it never reaches more than a few percent of the energy transport by bulk motion in the main part of the cooling zone. If there are small chaotic magnetic fields they could be frozen in the bulk motion of the material. They will further suppress thermal conduction which requires motion of particels relative to the bulk motion and accordingly perpendicular to this small-scale magnetic field. Due to the high temperatures all atoms are ionised and therefore all particles are charged and affected by magnetic fields. So the assumption of section 2.1.3 to neglect heat conduction is justified at the level of a few percent.

4.1.7 Deviation from equilibrium

In contrast to earlier works (Calvet and Gullbring 1998; Lamzin 1998) my simulation models the ionisation and recombination process and does not assume that the ions are always in collisional equilibrium. The code of CHIANTI 4.2 (Young et al. 2003) was modified to work with the calculated non-equilibrium ionisation instead of the tabulated equilibrium states, but strictly the atomic physics used is only valid for the assumption of local ionisation equilibrium (Porquet et al. 2001; Mewe and Schrijver 1978a,b). To quantify the deviation ΔI from equilibrium I define for element A:

$$\Delta I^A = \frac{1}{2} \sum_{\text{ionisation levels Z}} |x^A_{Z_{equilib}}(T) - x^A_{Z_{calc}}| \tag{4.4}$$

The factor $\frac{1}{2}$ normalises this quantity to unity. ΔI^A is shown for the shock parameters of table 4.1 for selected elements in figure 4.9. The ionisation cross sections and therefore the time scale to reach collisional ionisation equilibrium differs between elements. The largest discrepancies can be found directly behind the shock and close to the maximum depth. In the main cooling zone the difference is relatively small, in fact hydrogen and neon are so close to their collisional ionisation equilibrium that their lines are below x-axis in figure 4.9. Oxygen reaches the state of O VII

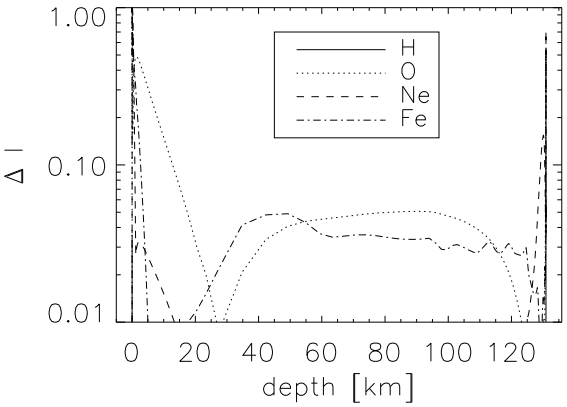

Figure 4.9: Difference of the ionisation state for selected elements to their equilibrium value for a typical shock (table 4.1). 0 means all ions are in their equilibrium state, 1 that all ions are in ionisation states which cannot be found in the corresponding collisional equilibrium.

immediately, it takes a bit longer to build up O VIII and even longer to get completely ionised. At a depth of 30 km the equilibrium state between these three ionisation stages is reached, which can be seen as very small ΔI^A in figure 4.9. The gas already cools down again and the oxygen recombines from here on. The cross section is so low that it is always more highly ionised than in equilibrium. As the density rises and the temperature drops the recombination accelerates and at 125 km nearly all oxygen is again in the state O VII which is close to its equilibrium value at this point. In the last few kilometers the hydrodynamic parameters change so quickly that all elements drop out of equilibrium again. For iron the structure is similar in the beginning, but between the depth of 95 km and 125 km there are some wiggles in the curve. They correspond to the region in figure 4.4 where iron recombines and quickly passes from Fe XIII to Fe IX. They should be regarded as numerical because the interpolation of the tabulated equilibrium values to a continuous temperature may already introduce errors on this scale.

4.2 Emission lines

Only the emission from the shock is directly observed. Therefore line ratios and line fluxes are vital to the analyses of observational data. Line ratios can deliver information on the density and temperature of the emitting region, because the abundance of the ions is temperature dependent. In hotter regions they will be higher ionised and the ratios of lines of different ionisation stages is a helpful tool to measure this. Unfortunately the elemental abundance of the infalling gas is not known a priory. Some authors suggest that it could be depleted of grain forming elements (Stelzer and Schmitt 2004; Argiroffi et al. 2005; Drake et al. 2005), so it is best to use different ions of the same element. Examples of this include the ratios of the Lyman α to the resonance line of the so called 'helium-like triplet' for Ne, O or N. The helium-like triplets offer a a temperature and density diagnostic which is even independent of the ionisation calculation. The basic atomic physics theory has been developed since the article Gabriel and Jordan (1969) by various authors. The most recent compilation is due to Porquet et al. (2001,see references therein for a more comprehensive literature listing). The helium-like triplet consists of the recombination line (label r, atomic transition $1s^2\ ^1S_0 - 1s2p\ ^1P_1$), the intercombination line (label i), which in fact again is a doublet of two close unresolvable lines (atomic transitions $1s^2\ ^1S_0 - 1s2p\ ^3P_{2,1}$), and the forbidden line (label f, atomic transition $1s^2\ ^1S_0 - 1s2p\ ^1S_1$). Two line ratios are widely used: One is density sensitive

$$R(n_{elec}) = \frac{f}{i} \tag{4.5}$$

and one is temperature sensitive

$$G(T_{elec}) = \frac{f+i}{r} \tag{4.6}$$

Unfortunately the line strengths and because of that the ratios change as a function of the background radiation field, too. For observational data this leads to some ambiguity between high densities and high background radiation fields. Nevertheless the helium-like triplets have proved

to be a useful tool in the analyses of T Tauri stars (Kastner et al. 2002; Stelzer and Schmitt 2004; Schmitt et al. 2005; Argiroffi et al. 2005).
Ratios between lines of different elements allow measurements of the relative elemental abundance and the emitted energy per area for any simulated line in comparison to measured values gives the size of the emitting region.

4.2.1 Origin of lines

In comparing different line ratios one has to be careful not to rely on too simple ideas. As I remarked earlier photons carry information about the physical conditions of the emitting region (e.g. about the electron density using the R-ratio from equation (4.5)), but not about its origin. If we compare ratios from different models, the regions, where the photons in question are mainly emitted, may be different. Figure 4.10 shows data for the Ne IX triplet from three simulations with different infall velocities. The x-axis is always labeled with normalised depth. The first row shows the relative abundance of the important neon ions. In the case $v_0 = 225$ km/s most Ne is not ionised up to Ne IX, which is helium-like. Only in the beginning the temperature is high enough to form it and it takes some time to reach the abundance maximum at depth ~ 0.3. With the higher velocity ($v_0 = 350$ km/s) a higher temperature is reached (see lower row of figure 4.10, where temperature and density profiles are shown) and nearly all Ne is in the form of Ne IX over the entire length of the cooling zone. With even more input energy ($v_0 = 500$ km/s) the ionisation to Ne IX occurs nearly instantly after passing through the shock front, but some neon is even ionised to Ne X and recombines later, so that near the end of the shock a second maximum in the Ne IX abundance is reached. The middle row shows the volume emissivity for the forbidden and the intercombination line of Ne IX. For small velocities the ratio probes the density at a small distance to the shock front, at $v_0 = 350$ km/s the emission peaks just behind the shock front, but has a tail extending up to the region of rapid recombination and in the high velocity case the emission is strong over the entire region because when the temperature drops and the line should get weaker the abundance of Ne IX increases due to recombining Ne X (see upper right panel of figure 4.10). Thus the line ratio observed includes density information integrated over the entire shock region. (The absolute scale of the emissivity is not the same for the three columns. It differs by several orders of magnitude due to a huge difference of the impacting kinetic energy.) The general procedure for comparison between simulation and observation must be to compare all observed lines to the emission integrated over the entire simulated shock to select the shock parameters realised.

4.2.2 Line ratios

Among the most useful line ratios are the R-ratio (equation 4.5) and the G-ratio (equation 4.6) for the helium-like triplets of oxygen and neon. For each model in the grid I calculate these ratios from the total line flux. Figure 4.11 shows contour plots for the R and G ratios for oxygen. In principle observations of just these two line ratios allow to find the infall velocity v_0 (using the G-ratio) and density n_0 (using the R-ratio) for any star, but if more line ratios are used the conclusions will be statistically more significant. The ratio f/i depends strongly on the background radiation field. The figure shows the ratio computed for three different background black-body radiation fields. The top three lines belong to the ratio 0.05. The difference between $T_{rad} = 6000$ K and $T_{rad} = 8000$ K is small, but the difference to the line for $T_{rad} = 10000$ K already noticeable. A v_0 and n_0 which results in a ratio of 0.3 with T_{rad} =6000 K show a ratio of only 0.1 for $T_{rad} = 10000$ K. f/i of 0.5 or higher cannot be produced if a background radiation with $T_{rad} = 10000$ K is present. This illustrates the problem that a small f/i ratio does not necessarily originate in a high density region, but could be a sign of strong UV-radiation. For neon the plots look similar, however the f/i ratio is only affected by stronger radiation fields with T_{rad} between 10000 K and 15000 K.

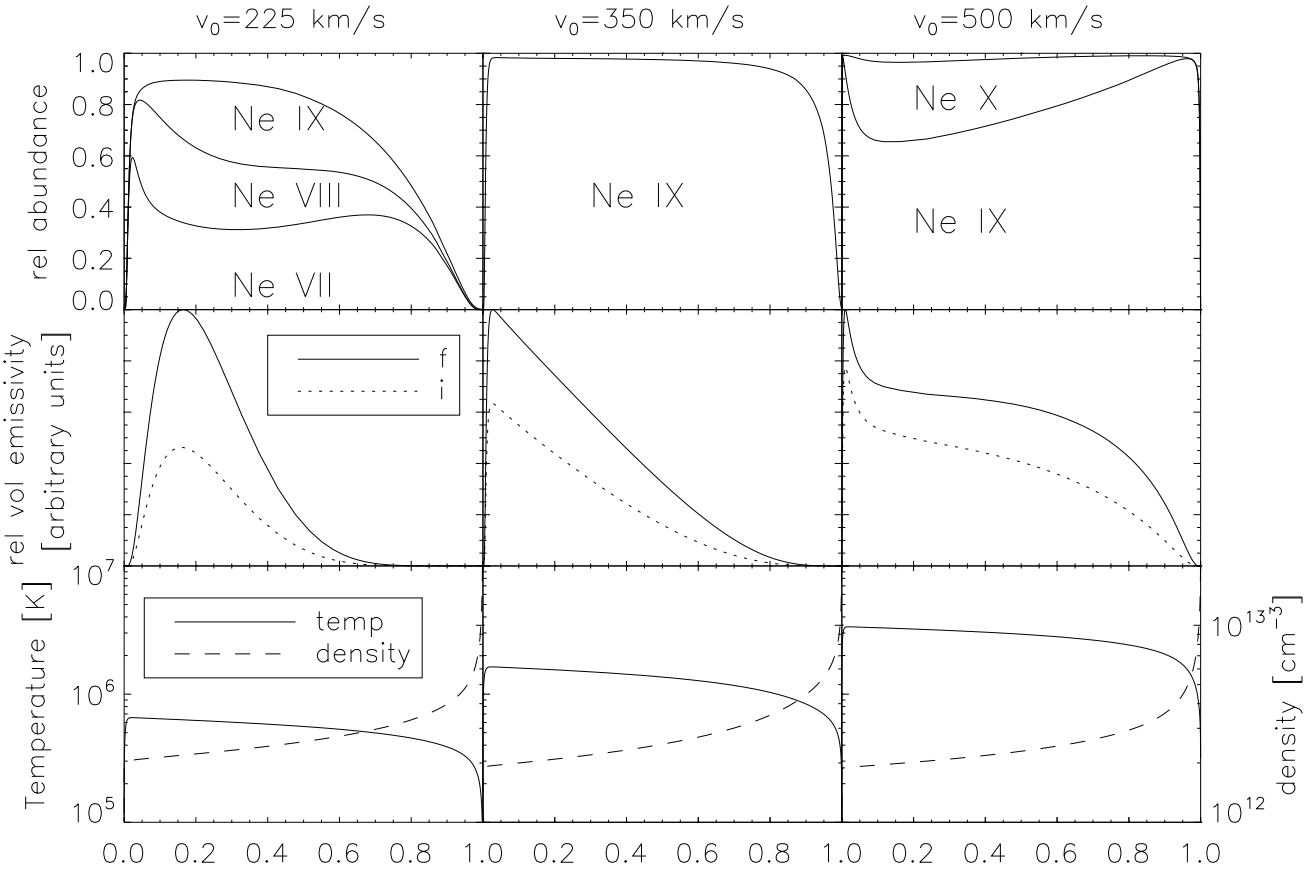

Figure 4.10: Each column shows results from a simulation with different infall velocity v_0. The x-axis is labelled by normalised depth, starting with 0 at the shock front. The first row shows the relative abundance of important Ne ions, the second the volume emissivity of the forbidden (dashed line) and intercombination (solid line) lines of the helium-like triplet Ne IX (in different arbitrary units for each column, because they differ by several orders of magnitude) and the third row the electron temperature [T_e in K] (solid line, left scale) and the ion density [n in cm^{-3}] (dashed line, right scale).

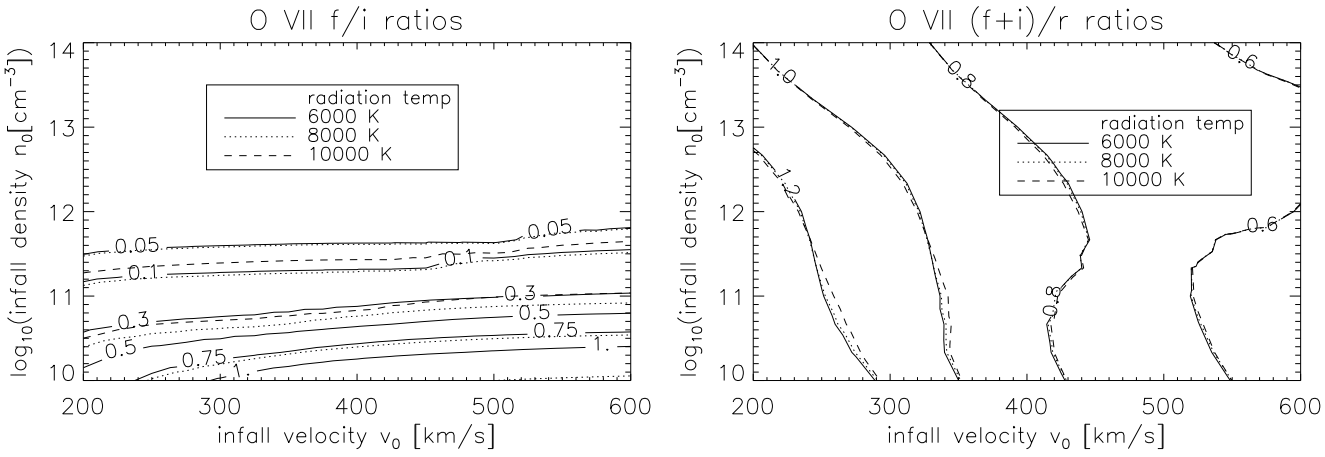

Figure 4.11: Simulated R (left) and G (right) ratios for oxygen. Both show contours for three different background radiation temperatures. For clarity only the contours for T_{rad} = 6000 K are labelled.

4.3 Application to TW Hya

TW Hya was identified as a CTTS early, but it is not submerged in a dark, molecular cloud like many other CTTS. TW Hya is the closest known CTTS, its distance is only 57 pc (Wichmann et al. 1998). Photospheric observations show variability between magnitude 10.9 and 11.3 in the V-band and broad Hα profiles (FWHM $\sim$ 200km/s) were observed by Rucinski and Krautter (1983) and Muzerolle et al. (2000), and it apparently belongs to a group of objects with similar age, the TW Hydrae association (TWA) (Webb et al. 1999). TW Hydrae's mass and radius are usually quoted as M_*=0.7 $M_\odot$, R_*=1.0 $R_\odot$ and the age as 10 Myr from Webb et al. (1999). These values carry considerable uncertainties because they are based on pre-main-sequence evolutionary tracks from D'Antona and Mazzitelli (1997), which carry uncertainties up to a factor of two by themselves. Using the 'typical error' from Webb et al. (1999) the age, for example, could be wrong by an order of magnitude. An alternative is given by Batalha et al. (2002), who place TW Hya on the HR-diagram from Baraffe et al. (1998) and determine stellar parameters from the optical spectrum, which fits an older (30 Myr) and smaller star (R_*=0.8 $R_\odot$). The spectral type of TW Hya is K7 V-M1 V (Webb et al. 1999; Batalha et al. 2002). The system is seen nearly face-on (Kastner et al. 1997; Wilner et al. 2000; Alencar and Batalha 2002). Moreover, TW Hya exhibits a hot wind (Dupree et al. 2005), which is likely driven by the same magnetic processes, which control the accretion (see e.g. Shu et al. 1994) and displays variations in the line profiles and the veiling, which have been interpreted as signs of rotation of an accretion spot (Alencar and Batalha 2002; Batalha et al. 2002). TW Hya has been observed in the UV with *IUE* and in the X-ray with *ROSAT* by Costa et al. (2000). After the advent of high-resolution X-ray satellites there have been two observations with *Chandra*/HETGS (Kastner et al. 2002) and with *XMM-Newton*/RGS (Stelzer and Schmitt 2004). I will use these observations as a basis for my analysis (see the references for details on the observations) and process both in parallel to check consistancy of my results.

4.3.1 Abundance independent line ratios
Infall velocity and density

As explained above ratios between lines of the same element allow to find the best model parameters independent of the elemental abundance.

Line ratio	S&S	Kastner	$v_0 = 525$	$v_0 = 575$
N R-ratio	0.30 ± 0.40		0.00	0.00
N G-ratio	0.58 ± 0.37		0.75	0.73
N Lymanα/N VIr	4.73 ± 2.30		2.70	3.26
O R-ratio	0.04 ± 0.06	0.00 ± 0.27	0.02	0.02
O G-ratio	0.56 ± 0.11	1.14 ± 0.70	0.72	0.69
O Lymanα/O VIIr	1.99 ± 0.30	2.44 ± 1.03	1.64	2.19
Ne R-ratio	0.47 ± 0.09	0.44 ± 0.12	0.33	0.32
Ne G-ratio	1.10 ± 0.13	0.93 ± 0.14	0.80	0.75
Ne Lymanα/Ne IXr	0.30 ± 0.08	0.67 ± 0.10	0.27	0.51
Fe XVII(17.09Å+17.05Å)/15.26Å		2.68 ± 1.26	4.92	4.62
Fe XVII17.09Å/17.05Å		0.71 ± 0.44	0.81	0.79

Table 4.2: The line ratios used in the fitting process for both observations are shown with their errors, S&S data is from Stelzer and Schmitt (2004), Kastner from Kastner et al. (2002). The two rightmost columns show results for the best-fit scenario from the simulation, the velocities of the models are given in km/s ($n_0 = 10^{12}$ cm^{-3} for both models).

The *XMM-Newton* data (Stelzer and Schmitt 2004) contains the helium-like triplets of N,O and Ne. For these three elements the Lyman α lines are included, too; I do not use the oxygen Lyman β line, because it is blended with an Fe XVIII line and relatively weak anyway. No strict fitting is carried out, I select the model from the grid which produces the smallest χ^2 in a standard weighted χ^2 maximum likelihood estimation (Press 2002). Since the measurement errors are not gaussian and the model, which is compared to the data, non-linear, the standard way to assign probabilities to χ^2 values is not valid. Poisson distributions produce more outliers then Gauß distributions, so the χ^2 values are expected to be higher than usual. Only a Monte-Carlo-simulation could provide the likelihood of the model.

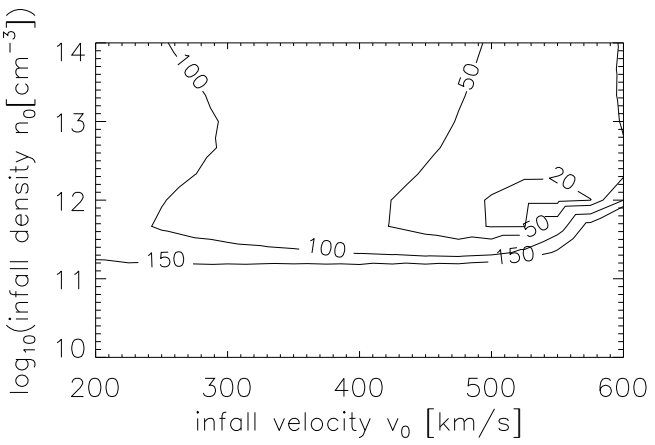

Figure 4.12: Contours are labelled with χ^2 values for TW Hya, data from Stelzer and Schmitt (2004)

Figure 4.12 shows the χ^2 values for a comparison between simulation and observation using nine line ratios (R-,G-ratio, Lymanα/r for N,O,Ne, see table 4.2). The best model has the parameters $v_0 = 525$ km/s and $n_0 = 10^{12}$ cm^{-3} with an unreduced $\chi^2 = 12.6$ (7 degrees of freedom), but figure 4.12 shows that a model with slightly lower v_0 and n_0 is also acceptable. Neon lines confine the fit strongest because they are observed with relatively high count rates and their values carry therefore only small statistical uncertainties. The density is restricted mainly by f/i ratios, the velocity by the Lyman α/r-ratio. One ratio does not quite fit the general picture. Figure 4.13 shows the simulated neon G-ratio. The observed value is 1.1 ± 0.13, which points to much lower infall velocities (the 1 σ range is dotted in the figure). If I fit the remaining eight ratios only I get very similar contour lines, but χ^2 is now only 6.4 (6 degrees of freedom). On the one hand this

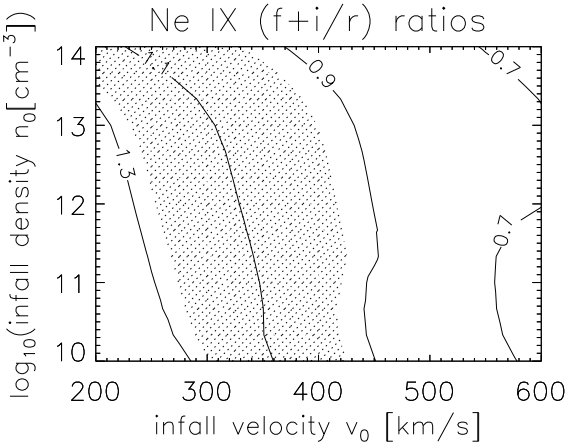

Figure 4.13: Simulated Neon G-ratios, the dotted area marks the observation $\pm 1\sigma$.

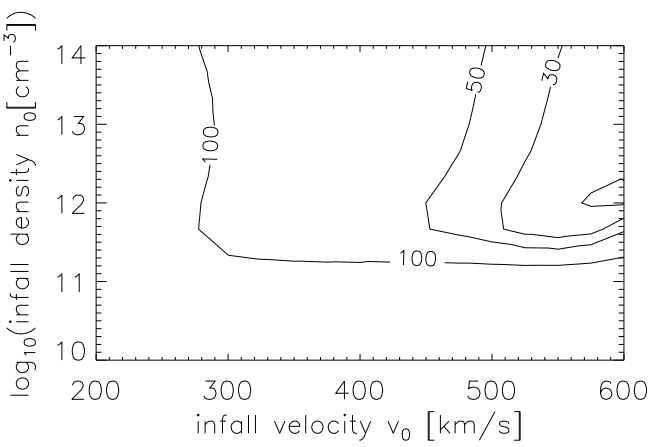

Figure 4.14: Contours are χ^2 values (10,30,50 and 100) for TW Hya, data from Kastner et al. (2002)

would be acceptable even for gaussian errors, on the other hand there is no obvious reason why the neon lines should have a behaviour which is different from nitrogen or oxygen. The fit does not depend on the background radiation temperature in the range 6000 K to 10000 K although the predicted f/i-ratio for oxygen changes.
The data from *Chandra* (Kastner et al. 2002) includes a different wavelength interval. Only the triplets from O and Ne are contained, but *Chandra* has a better resolution and this allows the measure several iron lines. I use the three lines of Fe XVII at 15.26 Å and the doublet at 17.05 Å and 17.09 Å, and calculate the ratio of the two doublet members and between their and the third line (see table 4.2). The contour lines for χ^2 are plotted in figure 4.14. The best fit model has $v_0 = 575$ km/s, which is slightly faster than before, and $n_0 = 10^{12}$ cm^{-3}, the same as the other data. The unreduced χ^2 is only 8.3 (6 degrees of freedom). Again there is no difference between 6000 K and 10000 K taken as temperature for a black-body radiation background. Like the other data the neon G-ratio points to lower infall velocities, although it is compatible with $v_0 = 400$ km/s, which is faster that for the first data set. Both fits have a tight lower bound on the density of the infalling gas. It cannot be much below $n_0 = 10^{12}$ cm^{-3}, but a slightly higher density or lower velocity is acceptable. I estimate the error as one grid point, that is ± 25 km/s for v and ± 0.33 for $\log(n_0)$ with n_0 in cm^{-3}.
The general model states that the gas impacts on the star with free fall velocity:

$$v_{free} = \sqrt{\frac{2GM_*}{R_*}} \approx 600 \sqrt{\frac{M_*}{M_\odot}} \sqrt{\frac{R_\odot}{R_*}} \frac{\text{km}}{\text{s}} \quad (4.7)$$

I evaluate this for the parameters from Webb et al. (1999) to 500 km/s and I get 550 km/s with the stellar radius from Baraffe et al. (1998). The equation 4.7 does not take into account that the gas is not coming from infinity, but from an surrounding disk, hence actually the velocity might be lower. This sets a tight upper bound and I take $v_0 = 525$ km/s from here on which is just large enough be be compatible with the fits persented earlier.

4.3.2 Element abundances

With fixed model parameters I can now compare the emissivities for two lines of different elements. I take the ratio between observation and simulation for each line and compare those ratios. Thus I can determine how the ratio of the two elements in question differs from the ratio the simulation is based on (Allen 1973). Unfortunately, this method does not deliver ab-

Element	Stelzer and Schmitt (2004)	Kastner et al. (2002)
C	0.25 ± 0.03	
N	0.7 ± 0.1	0.9 ± 0.2
O	0.33	0.33
Ne	4 ± 0.3	4 ± 1.0
Fe	0.27 ± 0.03	0.3 ± 0.06

Table 4.3: This table shows the abundance of elements relative to (Allen 1973). The errors are statistical only, I estimate the systematic error to 15%, oxygen carries no statistical error, because my method provides only ratios, which are all relative to oxygen.

solute abundances. Only carbon, nitrogen, oxygen, neon and iron have significant lines in this observed wavelength range. I do the calculation relative to oxygen, which offers four unblended lines (He-like-triplet and Lyman α). The data from Stelzer and Schmitt (2004) and Kastner et al. (2002) is consistent within the statistical errors (see table 4.3). Additionally, there are systematic errors, which include the uncertainty in the model parameters chosen; they probably dominate the statistical error from the line fitting. Neon is enhanced compared to oxygen by a factor of 12, nitrogen by a factor of 2-3, on the other side iron and carbon are slightly (by about a quarter) less abundant than in our local neighbourhood. I need to keep in mind that all these number are relative to oxygen. They are roughly in accordance with the numbers given in Kastner et al. (2002) and Stelzer and Schmitt (2004). These authors use the continuum for an absolute calibration. They conclude independently that oxygen is reduced compared to solar abundance by a factor of 3. I scale my analysis with this value and summarise my results in table 4.3.

The new abundances change the total emissivity of the plasma, because some lines get weaker and some stronger. So I did new simulations with the elemental abundance from Allen (1973) corrected by the factors in table 4.3 and went through the fitting procedure from section 4.3.1 again. The resulting values for n_0 and v_0 differ only by one grid point, which is the estimated model uncertainty. The shock structure is similar qualitatively, but the cooling length rises from ~ 600 km to ~ 950 km. All line ratios between ions of the same element agree within their errors with the original predictions, the total intensity, of course, now fits the new elemental abundances.

4.3.3 Filling factor and mass accretion rate

The simulation gives the integrated energy flux in a line per unit area. Taking the ratio between the observed energy flux f_{obs} (at the distance to the earth) and the simulated one f_{sim} per unit area (at the shock front) allows to calculate the accretion spot size A_{spot}. Ignoring interstellar extinction for the time being the total energy flux is conserved, but the flux per area decreases as the radiation dilutes for spherically symmetric emission:

$$4\pi d^2 f_{obs}(d) = A_{spot} f_{sim}(R_*)$$

Here d represents the distance between the star and the observer and R_* the stellar radius. This equation can be solved for the spot size

$$A_{spot} = \frac{f_{obs}(d)}{f_{sim}(R_*)} 4\pi d^2 \tag{4.8}$$

The filling factor f expresses the proportion of the stellar surface, that is covered by the spot:

$$f = \frac{A_{spot}}{4\pi R_*^2} = \frac{f_{obs}(d)}{f_{sim}(R_*)} \frac{d^2}{R_*^2} \tag{4.9}$$

To set bounds on the time scale of disk dispersal and to estimate the total energy, which can be released by accretion, the mass accretion rate is calculated. It is the product of the spot size and

the mass flux per unit area, which in turn is the product of the gas density $\rho_0 = \mu m_H n_0$ and the infall velocity v_0, conventionally the unit chosen for the mass flux is solar masses per year.

$$\frac{dM}{dt} = A_{spot}\rho v_0 = A_{spot}\mu m_H n_0 v_0 \qquad (4.10)$$

The formulae are applied to all unblended lines in the observations and the weighted average determined. The statistical errors are $\sim 10\%$, I estimate the systematical error to 15%. The spot size is then $6 - 7 \cdot 10^{19}$ cm^2, which yields filling factors of 0.1% and 0.2% for $R_* = 1\ R_\odot$ and $R_* = 0.8\ R_\odot$ respectively. The mass flux is about $1 \cdot 10^{-10}\ M_\odot$/yr.

Now it is possible to assess the hydrogen column density L_H, which the radiation passes between emission and observation. Depending on the position of the emitting atom three independent sources contribute: The interstellar hydrogen density, which is beyond the scope of this simulation, the pre-shock gas or the surrounding stellar atmosphere and the post-shock gas between the point of emission and the shock front (see illustrative figure 4.15). The total column density of the cooling zone is $L_{H_{post}} = 5 \cdot 10^{20}\mathrm{cm}^{-2}$, it increases nearly linearly from the shock front to the maximum depth because the density is nearly constant in the main cooling zone (see figure 4.16). Emission produced shortly behind the shock therefore passes less material. Then the radiation passes further material between the shock front and the interstellar space. Either it follows the path of the infalling matter or crosses the boundary between pre-shock gas and undisturbed stellar photosphere (see left panel of figure 4.16). Which possibility is realised to what proportion depends on the size of the spot. In the case of large spots most photons emitted outwards will be affected by extinction from the pre-shock material with

$$L_H \approx 10^{12}\mathrm{cm}^{-3} \cdot 1000\ \mathrm{km}\ \approx 10^{20}\mathrm{cm}^{-2}$$

The 1000 km are an estimate based on figure 4.7. The distance from the shock front to the point, where the stellar atmosphere has only a pressure of 100 dyn, can be read off there as about 500 km.

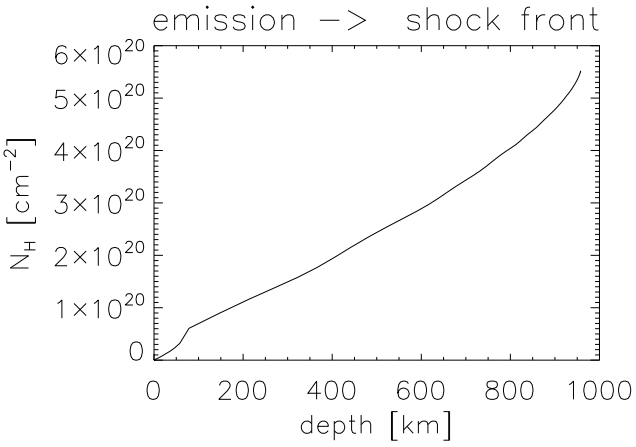

Figure 4.16: Column density L_H in cm^{-2} between shock front and point of emission, depth 0 km is the shock front

The accretion funnels curve (see section 1.2) and the radiation, propagating linearly, leaves the matter stream somewhere above the stellar surface, otherwise highly energetic radiation would be absorbed by ionising the infalling material before the shock completely (Lamzin 1995). If the radiation crosses the boundary to the stellar atmosphere it gets absorbed in a column density of more than 10^{21} cm^{-2}. In figure 4.17 (right panel) is shown the column density of the undisturbed

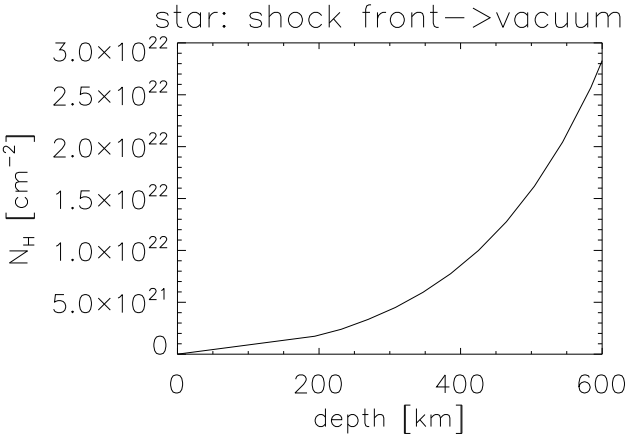

Figure 4.17: Column density L_H in cm^{-2} between interstellar space and the shock front, the shock front is at 500 km depth according to the *PHOENIX* model, see section 4.1.5

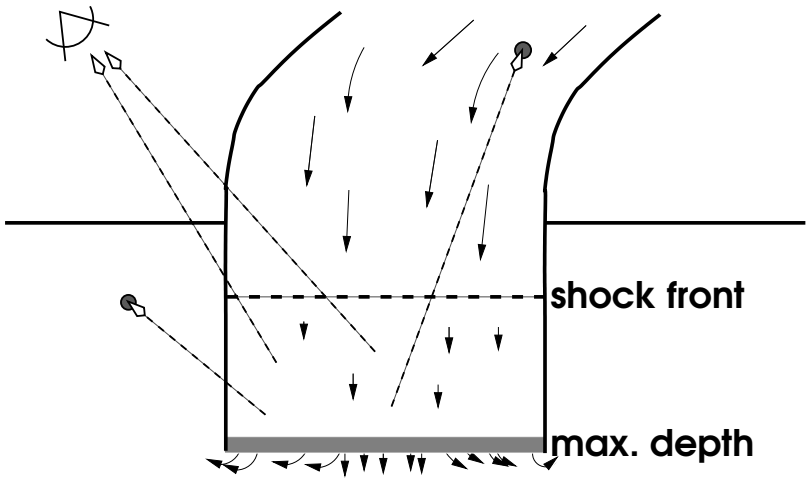

Figure 4.15: Illustration of different possible photon paths (dashed arrows) and examples where photons are absorbed

stellar atmosphere depends on the depth. The shock front is buried at about 500 km
A lower bound on the total column density is $L_H \approx 10^{20}$ cm^{-2} for a photon, which is emitted just behind the shock front and then penetrates the pre-shock gas.

4.4 Application to BP Tauri

BP Tau is a CTTS as evidenced by its excess continuum emission and by its Balmer emission (Bertout et al. 1988). It is a member of the Taurus-Auriga star forming region (distance $\sim$ 140 pc), where several TTS are located, Wichmann et al. (1998) argue this point because of common proper motion, although the *HIPPARCOS* paralax suggests BP Tau could be a single foreground star in a distance of 57 pc (further discussion in Drake et al. 2005). BP Tau's spectrum fits the type K7 and was studied extensively via optical monitoring by Gullbring et al. (1996), who found small variations on the time scale of hours with light curves different from solar flares. They interpret this as varying accretion rate. A consecutive simultaneous monitoring in the optical and the X-ray was carried out by Gullbring et al. (1997) over five nights and showed that variations in these bands are uncorrelated and led them to the conclusion that the X-ray emission is the result of normal activity and not a hot accretion spot.
Stellar parameters have been estimated for BP Tau in different articles. Simon et al. (2000) compare two different possibilities for mass determination. Placing the star on the pre-main-sequence evolutionary tracks from D'Antona and Mazzitelli (1997) they obtain $M_* = 0.7 M_\odot$, using dynamical observations of CO in the disk the resulting mass is higher: $M_* = 1.2 M_\odot$. The radius is estimated to 2-3 $R_\odot$ (Bertout et al. 1988; Muzerolle et al. 2003). According to equation (4.7) the free-fall velocity for BP Tau is then 450 km/s or 550 km/s depending on the value chosen for the mass.
BP Tau was after TW Hya the second CTTS to be observed with a high-resolution X-ray satelite. Schmitt et al. (2005) published the data I use here.
In the same manner as for TW Hya (see section 4.3.1 for details) abundance independent ratios are compared. Only neon and oxygen lines are strong enough here, for both elements Schmitt et al. (2005) give the line fluxes in the helium-like triplet and the Lymanα lines, for oxygen additionally in Lymanβ. Applying all possible ratios directly does not give a satisfactory fit. The $\chi^2 = 99$ (5 degrees of freedom) is unacceptable high and its contour lines point to shock densities and velocities far off scale as best model. Fitting

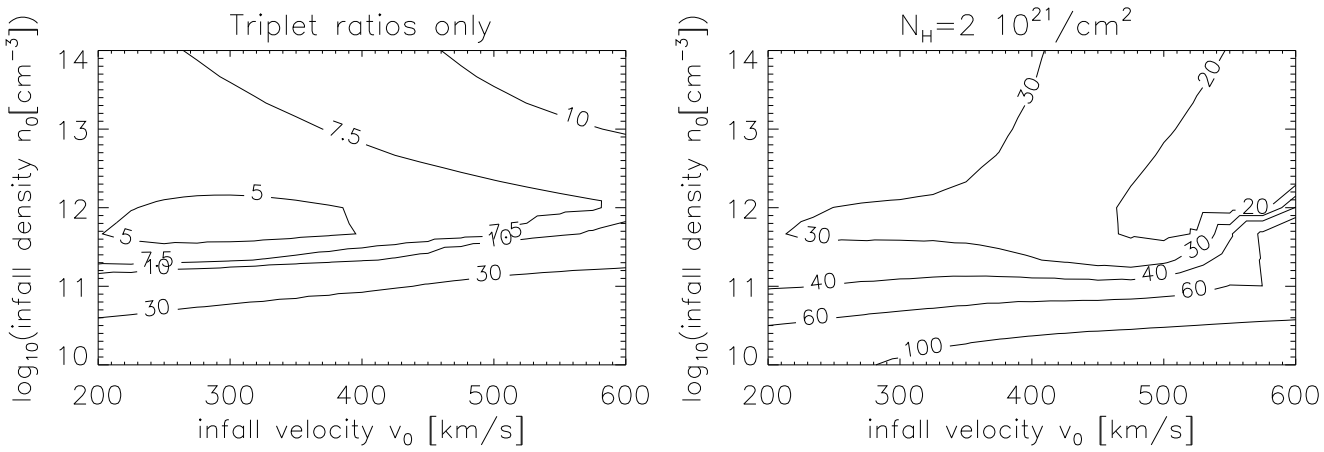

Figure 4.18: χ^2 values for BP Tau, data from Schmitt et al. (2005), using the helium-like triplet only (left) and additional Lymanα lines corrected for an absorbing column density.

	$L_H = 2 \cdot 10^{21}$ cm^{-2}		$L_H = 7 \cdot 10^{21}$ cm^{-2}	
Line ratio	Observation	Simulation	Observation	Simulation
O R-ratio	0.40 ± 0.18	0.02	0.48 ± 0.22	0.04
O G-ratio	1.16 ± 0.30	0.76	1.36 ± 0.36	0.87
O Lymanα/O VIIr	1.06 ± 0.28	1.05	0.27 ± 0.07	0.30
O Lymanα/Lymanβ	2.68 ± 0.76	8.42	6.59 ± 1.87	9.89
Ne R-ratio	0.39 ± 0.26	0.32	0.41 ± 0.27	0.58
Ne G-ratio	1.18 ± 0.46	0.86	1.24 ± 0.48	0.99
Ne Lymanα/Ne IXr	2.38 ± 0.71	0.10	1.58 ± 0.47	0.01

Table 4.4: This table shows the line ratios used in the fitting for BP Tau. The data is from Schmitt et al. (2005) and corrected for the extinction given in brackets. The corresponding best-fit scenarios from the simulation are printed for comparison. Their parameters are $v_0 = 475$ km/s and $n_0 = 10^{12}$ cm^{-3} and $v_0 = 400$ km/s and $n_0 = 10^{11.7}$ cm^{-3} respectively. For the fit of the left scenario the oxygen Lymanα to Lymanβ ratio was ignored.

just the R- and G-ratios of the triplets resembles a shock with the parameters $v_0 = 275$ km/s and $n_0 = 10^{11.7}$ cm^{-3} (see left panel figure 4.18), here χ^2 equals 4.0. One possible explanation is that emission from BP Tau passes an hydrogen column density of $L_H = 1 - 2 \cdot 10^{21}$ cm^{-2} (Hartigan et al. 1995; Gullbring et al. 1998; Robrade and Schmitt submitted), which affects different wavelengths in different ways. In this picture it is justified to use the triplet lines only because they have very similar wavelengths and suffer therefore from comparable extinction. To test on this I correct the observed fluxes with the method from Morrison and McCammon (1983) (with corrections in Balucinska-Church and McCammon (1992)) as it is implemented in the 'Package for Interactive Analyses of Line Emission (PINTofALE)' (Kashyap and Drake 2000). This correction lowers χ^2 to 54 (5 degrees of freedom). These high values indicate that the proposed model may not explain the emission from BP Tau.

Checking each line ratio on its own (see 4.4) reveals that especially the ratio oxygen Lymanβ to Lymanα presents problems. Ignoring this line delivers acceptable shock parameters:

$v_0 = 475$ km/s and $n_0 = 10^{12}$ cm^{-3} with $\chi^2 = 17$ (see right panel of figure 4.18 an table 4.4). With the method described in section 4.3.2 no reliable elemental abundance can be measured, the model does not fit the observations well enough, although it shows that neon is enhanced compared to oxygen. I take the abundances from Robrade and Schmitt (submitted) and the shock parameters presented above to estimate some shock properties. They carry considarable uncertainties and are only valid under the assumption that magnetically funnelled infall takes place on BP Tau at all. The best guess for these parameters is $f = 0.05\%$ and $2 - 3 \cdot 10^{-10}$ $M_\odot$/yr.

A shock with $v_0 = 275$ km/s as suggested by the helium-like triplet lines can be excluded because it requires a filling factor larger than unity to explain the total flux.

A second approach is to attribute the oxygen Lyβ to Lyα ratio to larger values for L_H. Using all available lines, but varying L_H shows that column densities above $L_H = 7 \cdot 10^{21}$ cm^{-2} fit the data with $\chi^2 \sim 20$ (ratios in table 4.4). The shock would have the infall parameters $v_0 = 400$ km/s and $n_0 = 10^{11.7}$ cm^{-3} in this case, this leads to a larger surface filling factor $f = 0.5\%$ and mass accretion rate of $2 \cdot 10^{-9}$ $M_\odot$/yr because the energy flux observed represents only a small fraction of energy emitted.

Chapter 5

Discussion

In this chapter I compare my results obtained in the previous sections for TW Hya and BP Tau to published literature values and discuss the deviations. For TW Hya the two basic issues are the metal depletion but neon enhancement observed and the mass accretion rate, which is determined differently using different wavelengths. This will be looked at in detail in section 5.2. In the case of BP Tau it is assumed that the X-ray emission is dominated by coronal activity which presents problems for the comparison to my simulation (section 5.3).

5.1 Simulation

As shown in section 4.1, my simulation produces a consistent picture of a shock. It agrees with previous calculations done independently by other authors (Lamzin 1998; Calvet and Gullbring 1998). Assumptions made in the beginning about the plane geometry and the thermal heat flux can be justified a posteriori. Other simplifications remain to be solved. To omit either the quasi-stationary condition or to include magnetic fields or turbulent flow requires a full more dimensional magneto-hydrodynamic (MHD) simulation. To extend the simulation to longer wavelengths is only possible if radiation transfer is calculated because in these regimes the optical depth will become important. The comparison to observational data in section 4.3 proves that all these complications are not necessary to reproduce the observed X-ray spectra.

5.2 TW Hydrae

The best fit between my simulation and the observations from TW Hya is obtained using a shock with the parameters $v_0 = (525 \pm 25)$ km/s and $\log(n_0) = 12 \pm 0.3$ (n_0 in cm^{-3}). Previous authors have assumed velocities closer to $\sim$ 300 km/s (Lamzin 1998; Calvet and Gullbring 1998). Observational evidence points to lower values, too. Stelzer and Schmitt (2004) convert their observed temperature into a velocity in a very simple way and they get $\sim$ 350 km/s. In the UV there are several lines with red wings, which extend up to $\sim$ 400 km/s (Lamzin et al. 2004), but then the gas accelerates strongly close to the stellar surface and because of particle number conservation the density will be lower in the high velocity region, so, depending on the geometry of the accretion funnel, it may well be that the emission measure in this region is very small. In this case the observed lines will have weak extensions to larger velocities, which are not identified observationally yet. So I regard these observation as a lower bound; an upper bound is provided by the free-fall velocity (equation 4.7) of $\sim 500 - 550$ km/s. The results from my simulation are compatible with both bounds and can be taken as input for the elemental abundance fitting procedure in section 4.3.2 reliably. The abundances measured agree well with previous analyses of the data used (Kastner et al. 2002; Stelzer and Schmitt 2004). A similar pattern of metal depletion has been observed in the wind by Lamzin et al. (2004) of TW Hya and it was also noted by Argiroffi et al. (2005) using X-ray observations of the quadruple system

TWA 5 in the vicinity of TW Hya. Stelzer and Schmitt (2004) interprete the abundances as a sign of grain depletion, where the grain forming elements condensate and mainly those elements which stay in the gas phase like the noble gas neon are accreted. This is discussed in detail by Drake et al. (2005) who collect evidence that metal depletion can be seen in the the infrared and UV, too, where the spectral distribution indicates well advanced coagulation into larger orbiting bodies which may resist the inward motion of the accreted gas (for details see references in that article).
Drake (2005) points to the absorption problem, but he believes that shocks are buried under $N_H > 10^{23}$ cm^{-2} because he disregards the possibility that photons pass through the thinner pre-shock gas and not the surrounding stellar atmosphere. In section 4.3.3 I discussed the hydrogen column density N_H which the photons emitted in the cooling zone pass on their way to the observer and estimated a lower limit of $L_H = 10^{20}$ cm^{-2}. The actually measured column density is $3.5 \cdot 10^{20}$ cm^{-2} (Robrade and Schmitt submitted). This even allows for situations where the photons have to penetrate more more pre-shock gas than I assumed or are emitted deeper inside the cooling zone. However the picture described (illustrated in figure 4.15) implies that the spots are located in regions of the stellar surface pointing towards the earth.

Measurements of TW Hya in different wavelength regions lead to conspicuously distinct mass accretion rates. Generally the estimates outdo my simulation, which gives the accretion rate $(1 \pm 0.25) \cdot 10^{-10}$ $M_\odot$/yr and the filling factor 0.1%-0.2%. In two articles Alencar and Batalha (2002) and Batalha et al. (2002) deploy optical spectroscopy and photometry, they state a mass accretion rate between 10^{-9} and 10^{-8} $M_\odot$/yr and a filling factor of a few percent. In the UV the picture is inconsistent. On the one hand two empirical relations for line intensities as accretion tracers (Johns-Krull et al. 2000) indicate mass accretion rate above $3 \cdot 10^{-8}$ $M_\odot$/yr (data from Valenti et al. (2000) evaluated by Kastner et al. (2002)), on the other hand fitting blackbodies on the UV-veiling by Muzerolle et al. (2000) suggests a significantly lower value: Only 0.3% of the surface area need to be covered by a spot to produce the observed accretion luminosity, this leads to the accretion rate $4 \cdot 10^{-10}$ $M_\odot$/yr. A similar procedure has been applied by Costa et al. (2000) earlier, but the estimated filling factor is 5% there. The previous X-ray analyses by Kastner et al. (2002) ($\frac{dM}{dt} = 10^{-8}$ $M_\odot$/yr) and Stelzer and Schmitt (2004) ($\frac{dM}{dt} = 10^{-11}$ $M_\odot$/yr) suffer from the problem that they use filling factors extracted from UV-measurements (from Costa et al. (2000) and Muzerolle et al. (2000) respectively) and a mass density calculated from X-ray observations which does not necessarily represent the same region. My simulation now is the first possibility rely on the X-ray only. The different values for mass accretion rates are summarised in figure 5.1.

The quoted estimates do not seem consistent with the assumption that the differences are purely statistical, but ask for a physical explanation. In longer wavelengths one observes plasma at cooler temperatures and in general the filling factor and mass accretion rates are higher. This can be solved naturally by an inhomogeneous spot with parts that impact with free-fall

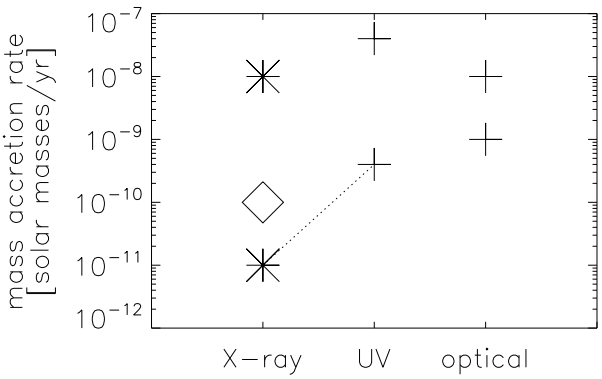

Figure 5.1: Estimated mass accretion rates. +: optical and UV measurements; *: X-ray, for the data from Stelzer and Schmitt (2004) the dotted line connects to the UV measurement, which delivers the filling factor, ◇: this simulation; data sources: see text

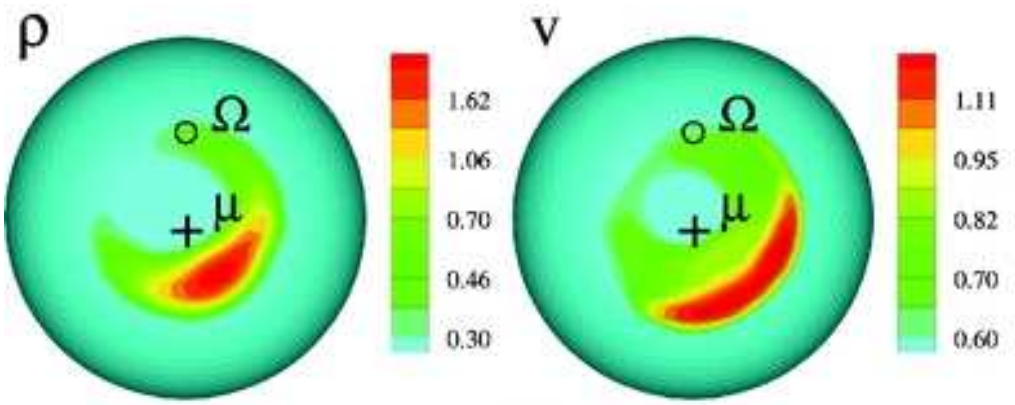

Figure 5.2: Accretion spots are not homogenous according to Romanova et al. (2004), μ marks the axis of the magnetic moment of the star, Ω its rotation axis, the angle between them is 30°. The density (left) and velocity (right) before the shock front are colour coded, their reference values are given in the text.

velocity and parts that are decelerated by magnetic or other processes. The fast particles would be responsible for a shock region with high temperatures which is observed in X-rays, whereas in other spectral bands cooler areas can be detected, too, and therefore the total area and the observed total mass flux is larger. Accretion spots with this kind of properties are predicted by the magneto-hydrodynamic simulations recently performed by Romanova et al. (2004). They concentrate on the geometry of the accretion funnel and the disk and do not perform simulation of the structure of the spot. The parameters they choose produce higher density spots (reference value $n_0 = 3 \cdot 10^{12}$) and slower infall velocities (reference value $v_0 = 300$ km/s). A cross section through the accretion funnel is shown in figure 5.2, which agrees with the considerations above.

5.3 BP Tauri

The results of the simulation for BP Tau are presented in section 4.4. They show that the underlying infall model does not describe the situation in BP Tau well. I tried already there to correct for an absorption column and this increases the quality of the fit. On the other hand simultaneous optical and X-ray observations show uncorrelated variations (Gullbring et al. 1997). Robrade and Schmitt (submitted) conclude that the X-ray activity from BP Tau is dominated by coronal activity, but has a contribution from accretion that explains the unusual f/i-ratios. All lines are then expected to be contaminated by a coronal contribution, although the lines originating in hotter regions, that is lines like Lymanα or Lymanβ, should be affected more than the triplet lines. In this picture variations are attributed to normal coronal activity like flares similar the one reported in Schmitt et al. (2005). Shock and coronal contributions cannot be disentangled from the observation, consequently the simulation has to be compared to the total emission, and of course a good fit cannot be expected. The best possibility is then to use $v_0 = 475$ km/s and $n_0 = 10^{12}$ cm^{-3}, which gives the lowest χ^2 and has the infall velocity close to free-fall. The estimated filling factor ($f = 0.05\%$) and mass accretion rate ($2 - 3 \cdot 10^{-10}$ $M_\odot$/yr) are then upper limits because they assume that all emission in the lines considered is produced in the shock front. Like for TW Hya the filling factor observed rises with larger wavelengths. Ardila and Basri (2000) measure $f_{UV} = 0.44\%$ using UV data from the IUE satelite and Calvet and Gullbring (1998) get $f_{opt/IR} = 0.7\%$ with optical and near-infrared data. They both determine a mass accretion rate $\sim 10^{-8} M_\odot$/yr. While this probably lends some support for the second sce-

nario in section 4.4, a large ($f = 0.5\%$) shock with a high absorption column, L_H is confined by other methods to $1 - 2 \cdot 10^{21}$ cm^{-2} (Robrade and Schmitt submitted). This simulation cannot distinguish between these alternatives, but due to the observation that the X-ray variations are not correlated to optical ones the first alternative seems more plausible, although it is an unsatisfying situation not to be able to determine exact shock properties because of the coronal component.

5.4 Summary

I presented a computer program, which simulates the accretion spot in CTTS. I derived the equations used and explained how the program is designed. The analysis of the simulation results clearly shows that the model of magnetically funnelled accretion explains the basic features in the X-ray emission of CTTS and a simulation without radiative transfer is adequate.

- The emission of TW Hya is dominated by accretion. The parameters of the pre-shock gas are determined from modelling the shock and comparing it to data to $v_0 = (525 \pm 25)$ km/s and $\log(n_0) = 12 \pm 0.3$ (n_0 in cm^{-3}).
- This allows to calculate the global parameters filling factor and mass accretion rate as $(1 \pm 0.25) \cdot 10^{-10}\ M_\odot$/yr and $f = 0.1 - 0.2$ %.
- Checking this with literature values shows that the size of the shock region depends on the wavelength where it is observed.
- In BP Tau coronal activity produces most of the X-ray emission, which clearly shows up in the high χ^2 values for the fits. Nevertheless BP Tau is a actively accreting CTTS and some emission is produced in a spot.
- From selected lines bounds on the properties of this shock are derived.
- This supports the thesis that accretion shock are a common feature on CTTS.
- New X-ray observations can now be converted easily into shock properties using the tools developed in the course of this diploma thesis, so to obtain a statistically significant sample of stars further high resolution observations of accreting stars are required.

Acknowledgements

The implementation of my program uses many routines of CHIANTI. CHIANTI is a collaborative project involving the NRL (USA), RAL (UK), MSSL (UK), the Universities of Florence (Italy) and Cambridge (UK), and George Mason University (USA).
This research has made use of NASA's Astrophysics Data System.

Some English words would be blank here without LEO, an online-dictionary operated by the Universität München.

I want to express my gratitude to Prof. J. H. M. M. Schmitt, who proposed the topic for this diploma thesis and coached me throughout its course and to his college Prof. P. Hauschildt, who advised me on some hydrodynamic problems and agreed to act as second corrector.

I thank my colleagues at the Hamburger Sternwarte. I found an excellent infrastructure there, especially in terms of office space and computing equipment. I had a very pleasent year and the people I met answered my questions patiently. Still some need to be emphasised, U. Wolter, because he shared his office with me and was the first person to be bothered with questions, B. Fuhrmeister, who advised me on some IDL problem and on my English expression and J. Robrade, who sacrificed his parts of his labour time nearly daily to explain X-rays and stars to me.

My family and my girlfirend are the last, not the least, on the list. They bear a physicist and always encouraged me to go on and do what I like.

Bibliography

S. H. P. Alencar and C. Batalha. Variability of Southern T Tauri Stars. II. The Spectral Variability of the Classical T Tauri Star TW Hydrae. *ApJ*, 571:378–393, May 2002.

F. Allard, P. H. Hauschildt, D. R. Alexander, A. Tamanai, and A. Schweitzer. The Limiting Effects of Dust in Brown Dwarf Model Atmospheres. *ApJ*, 556:357–372, July 2001.

C. W. Allen. *Astrophysical quantities*. London: University of London, Athlone Press, —c1973, 3rd ed., 1973.

D. R. Ardila and G. Basri. The Balmer Wavelength Range of BP Tauri. *ApJ*, 539:834–846, August 2000.

C. Argiroffi, A. Maggio, G. Peres, B. Stelzer, and R. Neuhäuser. XMM-Newton spectroscopy of the metal depleted T Tauri star TWA 5. *A&A*, 439:1149–1158, September 2005.

M. Arnaud and J. Raymond. Iron ionization and recombination rates and ionization equilibrium. *ApJ*, 398:394–406, October 1992.

M. Arnaud and R. Rothenflug. An updated evaluation of recombination and ionization rates. *A&AS*, 60:425–457, June 1985.

M. Balucinska-Church and D. McCammon. Photoelectric absorption cross sections with variable abundances. *ApJ*, 400:699–+, December 1992.

I. Baraffe, G. Chabrier, F. Allard, and P. H. Hauschildt. Evolutionary models for solar metallicity low-mass stars: mass-magnitude relationships and color-magnitude diagrams. *A&A*, 337:403–412, September 1998.

C. Batalha, N. M. Batalha, S. H. P. Alencar, D. F. Lopes, and E. S. Duarte. Variability of Southern T Tauri Stars (VASTT). III. The Continuum Flux Changes of the TW Hydrae Bright Spot. *ApJ*, 580:343–357, November 2002.

C. Bertout, G. Basri, and J. Bouvier. Accretion disks around T Tauri stars. *ApJ*, 330:350–373, July 1988.

N. S. Brickhouse. Systemization and Use of Atomic Data for Astrophysical Modeling. In *ASP Conf. Ser. 172: Astronomical Data Analysis Software and Systems VIII*, pages 25–+, 1999.

I. Brott and P. H. Hauschildt. A PHOENIX Model Atmosphere Grid for Gaia. In *ESA SP-576: The Three-Dimensional Universe with Gaia*, pages 565–+, January 2005.

D. D. Burgess, V. P. Myerscough, C. H. Skinner, and J. M. Ward. A comparison between theory and laser spectroscopic meassurements for a hydrogen plasma under high-intensity resonant Balmer line irridation. *J Phys. B*, 13: 1675–1701, 1980.

N. Calvet and E. Gullbring. The Structure and Emission of the Accretion Shock in T Tauri Stars. *ApJ*, 509:802–818, December 1998.

V. M. Costa, M. T. V. T. Lago, L. Norci, and E. J. A. Meurs. T Tauri stars: The UV/X-ray connection. *A&A*, 354:621–635, February 2000.

F. D'Antona and I. Mazzitelli. Evolution of low mass stars. *Memorie della Societa Astronomica Italiana*, 68:807–+, 1997.

G. del Zanna. CHIANTI: Application to X-ray High Resolution Spectroscopy. In *High Resolution X-ray Spectroscopy with XMM-Newton and Chandra*, December 2002.

K. P. Dere, E. Landi, H. E. Mason, B. C. M. Fossi, and P. R. Young. CHIANTI - an Atomic Database For Emission Lines Paper I: Wavelengths Greater than 50 Angstroms. In *ASP Conf. Ser. 143: The Scientific Impact of the Goddard High Resolution Spectrograph*, pages 390–+, 1998.

K. P. Dere, E. Landi, H. E. Mason, B. C. Monsignori Fossi, and P. R. Young. CHIANTI - an atomic database for emission lines. *A&AS*, 125:149–173, October 1997.

J. J. Drake. Trouble on the shock front: TW Hydrea, X-rays and accretion. In *13th Cambidge Workshop on Cool Stars, Stellar Systems and the Sun*, pages 519–523, 2005.

J. J. Drake, P. Testa, and L. Hartmann. X-Ray Diagnostics of Grain Depletion in Matter Accreting onto T Tauri Stars. *ApJ*, 627:L149–L152, July 2005.

A. K. Dupree, N. S. Brickhouse, G. H. Smith, and J. Strader. A Hot Wind from the Classical T Tauri Stars: TW Hydrae and T Tauri. *ApJ*, 625:L131–L134, June 2005.

S. Edwards, P. Hartigan, L. Ghandour, and C. Andrulis. Spectroscopic evidence for magnetospheric accretion in classical T Tauri stars. *AJ*, 108:1056–1070, September 1994.

E. D. Feigelson, S. Casanova, T. Montmerle, and J. Guibert. ROSAT X-Ray Study of the Chamaeleon I Dark Cloud. I. The Stellar Population. *ApJ*, 416:623–+, October 1993.

E. D. Feigelson and W. M. Decampli. Observations of X-ray emission from T Tauri stars. *ApJ*, 243:L89–L93, January 1981.

E. D. Feigelson and G. A. Kriss. Soft X-ray observations of pre-main-sequence stars in the Chamaeleon dark cloud. *ApJ*, 338:262–276, March 1989.

E. D. Feigelson and T. Montmerle. High-Energy Processes in Young Stellar Objects. *ARA&A*, 37:363–408, 1999.

A. H. Gabriel and C. Jordan. Interpretation of solar helium-like ion line intensities. *MNRAS*, 145:241–+, 1969.

A. E. Glassgold, E. D. Feigelson, and T. Montmerle. Effects of Energetic Radiation in Young Stellar Objects. *Protostars and Planets IV*, pages 429–+, May 2000.

J. Gregorio-Hetem, T. Montmerle, S. Casanova, and E. D. Feigelson. X-rays and star formation: ROSAT observations of the Monoceros and Rosette molecular clouds. *A&A*, 331:193–210, March 1998.

E. Gullbring, H. Barwig, P. S. Chen, G. F. Gahm, and M. X. Bao. Activity on the classical T Tauri star BP Tauri. *A&A*, 307:791–802, March 1996.

E. Gullbring, H. Barwig, and J. H. M. M. Schmitt. Simultaneous optical and ROSAT X-ray observations of the classical T Tauri star BP Tauri. *A&A*, 324:155–160, August 1997.

E. Gullbring, N. Calvet, J. Muzerolle, and L. Hartmann. The Structure and Emission of the Accretion Shock in T Tauri Stars. II. The Ultraviolet-Continuum Emission. *ApJ*, 544: 927–932, December 2000.

E. Gullbring, L. Hartmann, C. Briceno, and N. Calvet. Disk Accretion Rates for T Tauri Stars. *ApJ*, 492:323–+, January 1998.

P. Hartigan, S. Edwards, and L. Ghandour. Disk Accretion and Mass Loss from Young Stars. *ApJ*, 452:736–+, October 1995.

L. Hartmann. *Accretion Processes in Star Formation*. Accretion processes in star formation / Lee Hartmann. Cambridge, UK ; New York : Cambridge University Press, 1998. (Cambridge astrophysics series ; 32) ISBN 0521435072., June 1998.

C. M. Johns-Krull, J. A. Valenti, and J. L. Linsky. An IUE Atlas of Pre-Main-Sequence Stars. II. Far-Ultraviolet Accretion Diagnostics in T Tauri Stars. *ApJ*, 539:815–833, August 2000.

J. S. Kaastra. Astrophysical Plasmas; Atomic Processes. In *IAU Symp. 188: The Hot Universe*, pages 43–+, 1998.

V. Kashyap and J. J. Drake. PINTofALE : Package for the interactive analysis of line emission. *Bulletin of the Astronomical Society of India*, 28:475–476, June 2000.

J. H. Kastner, D. P. Huenemoerder, N. S. Schulz, C. R. Canizares, and D. A. Weintraub. Evidence for Accretion: High-Resolution X-Ray Spectroscopy of the Classical T Tauri Star TW Hydrae. *ApJ*, 567:434–440, March 2002.

J. H. Kastner, B. Zuckerman, D. A. Weintraub, and T. Forveille. X-ray and molecular emission from the nearest region of recent star formation. *Science*, 277:67–71, 1997.

A. Koenigl. Disk accretion onto magnetic T Tauri stars. *ApJ*, 370:L39–L43, March 1991.

A. Konigl and R. E. Pudritz. Disk Winds and the Accretion-Outflow Connection. *Protostars and Planets IV*, pages 759–+, May 2000.

S. A. Lamzin. On the structure of the accretion shock wave in the case of young stars. *A&A*, 295:L20–L22, March 1995.

S. A. Lamzin. The structure of shock waves in the case of accretion onto low-mass young stars. *Astronomy Reports*, 42:322–335, May 1998.

S. A. Lamzin, A. S. Kravtsova, M. M. Romanova, and C. Batalha. Kinematics and Parameters of the Gas in the Vicinity of TW Hya. *Astronomy Letters*, 30:413–427, June 2004.

E. Landi, U. Feldman, and K. P. Dere. CHIANTI-An Atomic Database for Emission Lines. V. Comparison with an Isothermal Spectrum Observed with SUMER. *ApJS*, 139: 281–296, March 2002.

E. et al. Landi. in press. *ApJS*, in press.

M. Landini and B. C. Monsignori Fossi. The X-UV spectrum of thin plasmas. *A&AS*, 82:229–260, February 1990.

M. Landini and B. C. Monsignori Fossi. Ion equilibrium for minor components in a thin plasma. *A&AS*, 91:183–196, November 1991.

P. Mazzotta, G. Mazzitelli, S. Colafrancesco, and N. Vittorio. Ionization balance for optically thin plasmas: Rate coefficients for all atoms and ions of the elements H to NI. *A&AS*, 133: 403–409, December 1998.

H. Meller. Die Himmelsscheibe von Nebra. Fundgeschichte und archäologische Bewertung. *Archäologie in Sachsen-Anhalt*, 1:7–31, 2002.

R. Mewe, J. R. Lemen, and G. H. J. van den Oord. Calculated X-radiation from optically thin plasmas. VI - Improved calculations for continuum emission and approximation formulae for nonrelativistic average Gaunt factors. *A&AS*, 65:511–536, September 1986.

R. Mewe and J. Schrijver. Heliumlike Ion Line Intensities. II Non-stationary Plasmas. *A&A*, 65:115–+, April 1978a.

R. Mewe and J. Schrijver. Heliumlike ion line intensities. III - Results. *A&AS*, 33:311–313, September 1978b.

R. Morrison and D. McCammon. Interstellar photoelectric absorption cross sections, 0.03-10 keV. *ApJ*, 270:119–122, July 1983.

J. Muzerolle, N. Calvet, C. Briceño, L. Hartmann, and L. Hillenbrand. Disk Accretion in the 10 MYR Old T Tauri Stars TW Hydrae and Hen 3-600A. *ApJ*, 535: L47–L50, May 2000.

J. Muzerolle, N. Calvet, and L. Hartmann. Magnetospheric Accretion Models for the Hydrogen Emission Lines of T Tauri Stars. *ApJ*, 492:743–+, January 1998a.

J. Muzerolle, N. Calvet, L. Hartmann, and P. D'Alessio. Unveiling the Inner Disk Structure of T Tauri Stars. *ApJ*, 597:L149–L152, November 2003.

J. Muzerolle, L. Hartmann, and N. Calvet. A Brgamma Probe of Disk Accretion in T Tauri Stars and Embedded Young Stellar Objects. *AJ*, 116:2965–2974, December 1998b.

R. Neuhaeuser, M. F. Sterzik, J. H. M. M. Schmitt, R. Wichmann, and J. Krautter. ROSAT survey observation of T Tauri stars in Taurus. *A&A*, 297:391–+, May 1995.

D. Pequignot, P. Petitjean, and C. Boisson. Total and effective radiative recombination coefficients. *A&A*, 251:680–688, November 1991.

D. Porquet, R. Mewe, J. Dubau, A. J. J. Raassen, and J. S. Kaastra. Line ratios for helium-like ions: Applications to collision-dominated plasmas. *A&A*, 376:1113–1122, September 2001.

W. H. Press. *Numerical recipes in C++ : the art of scientific computing*. Numerical recipes in C++ : the art of scientific computing by William H. Press. xxviii, 1,002 p. : ill. ; 26 cm. Includes bibliographical references and index. ISBN : 0521750334, 2002.

J. C. Raymond. Radiation from Hot, Thin Plasmas. In *NATO ASIC Proc. 249: Hot Thin Plasmas in Astrophysics*, pages 3–+, 1988.

J. Robrade and J. H. M. M. Schmitt. XMM-Newton X-ray spectroscopy of classical T Tauri stars. *A&A*, submitted.

M. M. Romanova, G. V. Ustyugova, A. V. Koldoba, and R. V. E. Lovelace. Three-dimensional Simulations of Disk Accretion to an Inclined Dipole. II. Hot Spots and Variability. *ApJ*, 610:920–932, August 2004.

S. M. Rucinski and J. Krautter. TW Hya - A T Tauri star far from any dark cloud. *A&A*, 121: 217–225, May 1983.

J. H. M. M. Schmitt, J. Robrade, J.-U. Ness, F. Favata, and B. Stelzer. X-rays from accretion shocks in T Tauri stars: The case of BP Tau. *A&A*, 432:L35–L38, March 2005.

F. Shu. *Physics of Astrophysics, Vol. II: Gas Dynamics*. Published by University Science Books, 648 Broadway, Suite 902, New York, NY 10012, 1991., 1991.

F. Shu, J. Najita, E. Ostriker, F. Wilkin, S. Ruden, and S. Lizano. Magnetocentrifugally driven flows from young stars and disks. 1: A generalized model. *ApJ*, 429:781–796, July 1994.

F. H. Shu, J. R. Najita, H. Shang, and Z.-Y. Li. X-Winds Theory and Observations. *Protostars and Planets IV*, pages 789–+, May 2000.

J. M. Shull and M. van Steenberg. The ionization equilibrium of astrophysically abundant elements. *ApJS*, 48:95–107, January 1982.

M. Simon, A. Dutrey, and S. Guilloteau. Dynamical Masses of T Tauri Stars and Calibration of Pre-Main-Sequence Evolution. *ApJ*, 545:1034–1043, December 2000.

R. K. Smith, N. S. Brickhouse, D. A. Liedahl, and J. C. Raymond. Collisional Plasma Models with APEC/APED: Emission-Line Diagnostics of Hydrogen-like and Helium-like Ions. *ApJ*, 556:L91–L95, August 2001.

L. Spitzer. *Physics of fully ionized gases*. Interscience Tracts on Physics and Astronomy, New York: Interscience Publication, 1965, 2nd rev. ed., 1965.

B. Stelzer and J. H. M. M. Schmitt. X-ray emission from a metal depleted accretion shock onto the classical T Tauri star TW Hya. *A&A*, 418:687–697, May 2004.

Y. Uchida. Magnetic accretion model for the activities of very young stars. In *ASSL Vol. 102: IAU Colloq. 71: Activity in Red-Dwarf Stars*, pages 625–+, 1983.

J. A. Valenti, C. M. Johns-Krull, and J. L. Linsky. An IUE Atlas of Pre-Main-Sequence Stars. I. Co-added Final Archive Spectra from the SWP Camera. *ApJS*, 129:399–420, July 2000.

D. A. Verner and G. J. Ferland. Atomic Data for Astrophysics. I. Radiative Recombination Rates for H-like, He-like, Li-like, and Na-like Ions over a Broad Range of Temperature. *ApJS*, 103:467–+, April 1996.

D. A. Verner and D. G. Iakovlev. Photoionization models for QSO's intervening absorption clouds. *Ap&SS*, 165:27–40, March 1990.

G. S. Voronov. A Practical Fit Formula for Ionization Rate Coefficients of Atoms and Ions by Electron Impact: Z = 1-28. *Atomic Data and Nuclear Data Tables*, 65:1–+, 1997.

R. A. Webb, B. Zuckerman, I. Platais, J. Patience, R. J. White, M. J. Schwartz, and C. McCarthy. Discovery of Seven T Tauri Stars and a Brown Dwarf Candidatein the Nearby TW Hydrae Association. *ApJ*, 512:L63–L67, February 1999.

R. Wichmann, U. Bastian, J. Krautter, I. Jankovics, and S. M. Rucinski. HIPPARCOS observations of pre-main-sequence stars. *MNRAS*, 301:L39+, December 1998.

D. J. Wilner, P. T. P. Ho, J. H. Kastner, and L. F. Rodríguez. VLA Imaging of the Disk Surrounding the Nearby Young Star TW Hydrae. *ApJ*, 534:L101–L104, May 2000.

P. R. Young, G. Del Zanna, E. Landi, K. P. Dere, H. E. Mason, and M. Landini. CHIANTI-An Atomic Database for Emission Lines. VI. Proton Rates and Other Improvements. *ApJS*, 144:135–152, January 2003.

P. R. Young, E. Landi, and R. J. Thomas. CHIANTI: an atomic database for emission lines. II. Comparison with the SERTS-89 active region spectrum. *A&A*, 329:291–314, January 1998.

Y. B. Zel'Dovich and Y. P. Raizer. *Physics of shock waves and high-temperature hydrodynamic phenomena*. New York: Academic Press, 1966/1967, edited by Hayes, W.D.; Probstein, Ronald F., 1967.